

¹ Susceptible host dynamics explain pathogen resilience to
² perturbations

⁴
⁵ Sang Woo Park,^{1,*} Bjarke Frost Nielsen² Emily Howerton² Bryan T. Grenfell,²
⁶ Sarah Cobey^{2,3,4} Sarah Cobey¹

⁷ ¹ Department of Ecology and Evolution, University of Chicago, Chicago, IL, USA

⁸ ² Department of Ecology and Evolutionary Biology, Princeton University,
Princeton, NJ, USA

¹⁰ ³ High Meadows Environmental Institute, Princeton University, Princeton, NJ,
USA

¹² ⁴ Princeton School of Public and International Affairs, Princeton, NJ, USA

¹³ *Corresponding author: swp2@uchicago.edu

¹⁴ Abstract

¹⁵ A major priority for epidemiological research in ~~the a~~ time of anthropogenic change
¹⁶ is understanding how infectious disease dynamics respond to perturbations. Inter-
¹⁷ ventions to slow the spread of SARS-CoV-2 significantly disrupted the transmission
¹⁸ of other human pathogens. As interventions lifted, whether and when respiratory
¹⁹ pathogens would eventually return to their pre-pandemic dynamics remains to be
²⁰ answered. Here, we present a framework for estimating pathogen resilience based on
²¹ how fast epidemic patterns ~~return to approach~~ their pre-pandemic, endemic dynam-
²² ics and analyze ~~relevant~~ time series data from Hong Kong, Canada, Korea, and the
²³ US~~from the resulting framework~~. By quantifying the resilience of common respira-
²⁴ tory pathogens, we are able to predict when each pathogen will eventually return to
²⁵ ~~its~~ pre-pandemic, ~~endemic~~ dynamics. Our predictions ~~about whether each pathogen~~
²⁶ ~~should have already returned to its pre-pandemic dynamics~~ closely match the ob-
²⁷ served ~~patterns of~~ deviations (or lack thereof) from ~~its pre-pandemic dynamics the~~
²⁸ ~~pre-COVID dynamics of respiratory pathogens~~. Discrepancies between predicted
²⁹ and observed dynamics indicate the long-term ~~impact impacts~~ of pandemic per-
³⁰ turbations, suggesting ~~a possibility~~ that some pathogens may ~~have converged be~~
³¹ ~~converging~~ to a different endemic cycle. Finally, we show that the replenishment
³² rate of the susceptible pool is a key determinant of pathogen resilience, which in
³³ turn determines the sensitivity of a system to stochastic perturbations. Overall, our
³⁴ analysis highlights the persistent nature of common respiratory pathogens ~~compared~~
³⁵ ~~to vaccine-preventable infections, such as measles~~.

Introduction

Non-pharmaceutical interventions to slow the spread of SARS-CoV-2 disrupted the transmission of other human respiratory pathogens, adding uncertainties to their future epidemic dynamics and ~~the overall their~~ public health burden [1]. As interventions lifted, large heterogeneities in outbreak dynamics were observed across different pathogens in different countries, with some pathogens exhibiting earlier and faster resurgences than others [2, 3, 4]. Heterogeneities in the overall reduction in transmission and the timing of re-emergence likely reflect differences in intervention patterns, pathogen characteristics, immigration/importation from other countries, and pre-pandemic pathogen dynamics [5]. Therefore, comparing the differential impact of the pandemic perturbations across pathogens can provide unique opportunities to learn about underlying pathogen characteristics, such as their transmissibility or duration of immunity, from heterogeneities in re-emergence patterns [6].

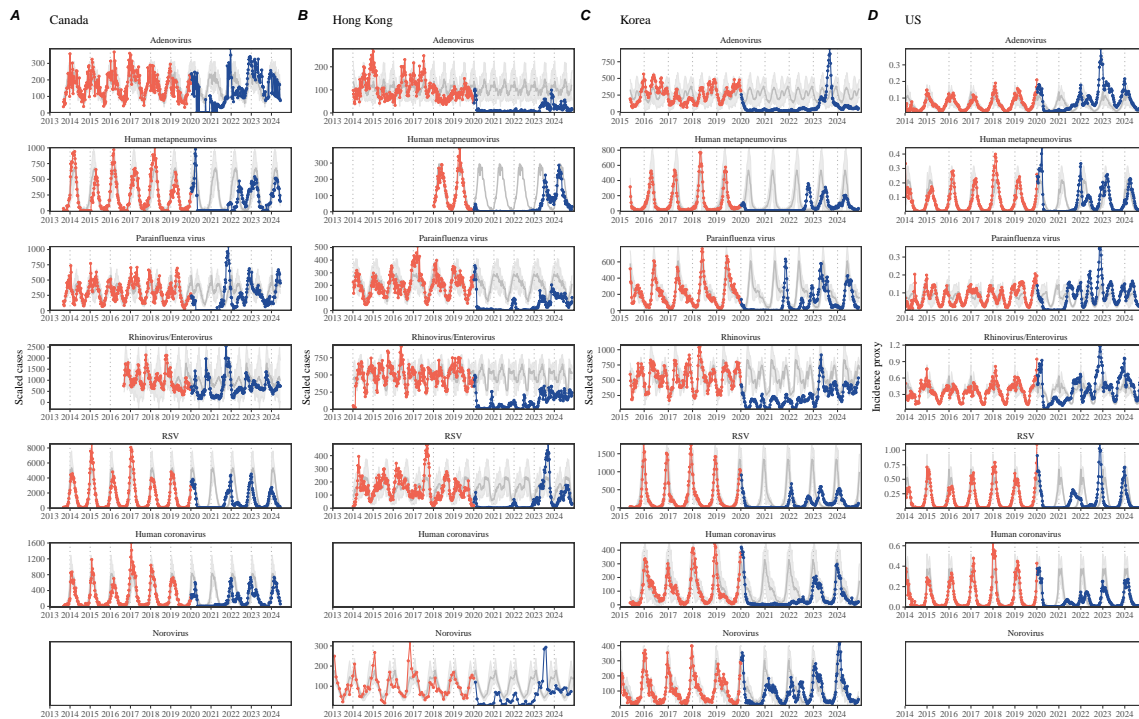


Figure 1: Observed heterogeneity in responses to pandemic perturbations across respiratory pathogens and norovirus in (A) Canada, (B) Hong Kong, (C) Korea, and (D) US. Red points and lines represent data before 2020. Blue points and lines represent data since 2020. Gray lines and shaded regions represent the mean seasonal patterns and corresponding 95% confidence intervals around the mean. Mean seasonal patterns were calculated by aggregating cases before 2020 into 52 weekly bins and taking the average in each week. Cases were scaled to account for changes in testing patterns (Materials and Methods).

49 Even though more than five years have passed since the emergence of SARS-CoV-
50 2, we still observe persistent changes in pathogen dynamics following the pandemic
51 perturbations. For example, compared to pre-pandemic, seasonal patterns, human
52 metapneumovirus in Korea ~~seem~~seems to circulate at lower levels, whereas RSV in
53 Korea seems to exhibit different seasonality (Figure 1). These observations suggest a
54 possibility ~~for a fundamental of a long-term~~ change in pathogen dynamics following
55 the pandemic perturbations, which ~~can might~~ be driven by a ~~permanent~~long-term
56 shift in either human behavior or population-level immunity [7, 8]. For example, the
57 emergence of SARS-CoV-2 could have caused a long-term shift in population-level
58 immunity through its interactions with other pathogens [9], especially with seasonal
59 coronaviruses [7, 10, 11]. The possibility of a long-lasting impact of the pandemic
60 perturbations poses an important question for future infectious disease dynamics:
61 can we predict whether and when other ~~respiratory~~ pathogens will eventually return
62 to their pre-pandemic dynamics?

63 So far, ~~the majority of epidemiological~~most analyses of respiratory pathogens in
64 the context of the ~~after~~ pandemic perturbations have focused on characterizing the
65 timing of rebound [1, 12, 5]. Instead, we seek to characterize how fast (and whether)
66 a pathogen returns to its pre-pandemic dynamics. These two concepts have a subtle
67 but important ~~differences~~: for difference. For example, it took more than 3 years
68 for human metapneumovirus to rebound in Hong Kong, but the observed epidemic
69 patterns in 2024 are appear similar to pre-pandemic seasonal means, suggesting a
70 ~~rapid~~possible return to pre-pandemic dynamics~~following a perturbation~~, though
71 confirmation may require multiple seasons (Figure 1). Measuring this rate of return
72 is ~~particularly~~ useful because it allows us to quantify the ecological resilience of a host-
73 pathogen system, which can inform responses to future interventions [13, 14, 15, 16].

74 In this study, we lay out theoretical and statistical approaches to characterizing
75 the resilience of a host-pathogen system based on how fast the system recovers from
76 perturbation. We begin by laying out a few representative scenarios that capture
77 the potential impact of pandemic perturbations on endemic pathogen dynamics and
78 illustrate how resilience can be measured by comparing the pre- and post-pandemic
79 dynamics of susceptible and infected hosts. In practice, information on suscepti-
80 ble hosts is often unavailable, making this theoretical approach infeasible. Instead,
81 we utilize a mathematical technique to reconstruct empirical attractors from the
82 data [17], which allows us to measure the rate at which the host-pathogen system
83 approaches this empirical attractor after a perturbation; ~~this rate corresponds to~~
84 the we define this rate to be the empirical resilience of the host-pathogen system.
85 We use this method to analyze pathogen surveillance data for respiratory and non-
86 respiratory pathogens from Canada, Hong Kong, Korea, and the US. Finally, we show
87 that susceptible host dynamics explain variation in pathogen resilience and further
88 ~~link pathogen resilience to responses to demonstrate that more resilient pathogens~~
89 will be less sensitive to perturbations caused by demographic stochasticity, thereby
90 providing a direct link between pathogen resilience and persistence.

⁹¹ Conceptual introduction to pathogen resilience

⁹² In the classical ecological literature, the resilience of an ecological system is mea-
⁹³ sured by the rate at which the system returns to its reference state following a
⁹⁴ perturbation [13, 14, 15, 16]. This rate corresponds to the largest real part of the
⁹⁵ eigenvalues of the linearized system near equilibrium—here, we refer to this value
⁹⁶ as the *intrinsic* resilience of the system, which represents the expected rate of re-
⁹⁷ turn from perturbed states. In practice, we rarely know the true model describing
⁹⁸ population-level dynamics of common respiratory pathogens, limiting our ability to
⁹⁹ infer the intrinsic resilience of a system. Instead, we can ~~still~~ measure the *empirical*
¹⁰⁰ resilience of a host-pathogen system by looking at how fast the system returns to the
¹⁰¹ ~~pre-pandemic~~^{pre-perturbation}, endemic dynamics after ~~pandemic perturbations are~~
¹⁰² ~~lifted~~^{the perturbation has ended.} The COVID-19 pandemic provides a particularly
¹⁰³ useful example of a major perturbation, providing unique opportunities to measure
¹⁰⁴ the resilience of a host-pathogen system.

¹⁰⁵ Resilience of a single-strain system under a short-term perturbation.

¹⁰⁶ As an example, we begin with a simple Susceptible-Infected-Recovered-Susceptible
¹⁰⁷ (SIRS) model with seasonally forced transmission and demography (i.e., birth and
¹⁰⁸ death). The SIRS model is the simplest model that allows for the waning of immunity
¹⁰⁹ and is commonly used for modeling the dynamics of respiratory pathogens [18]. First,
¹¹⁰ consider a pandemic perturbation that reduces transmission by 50% for 6 months
¹¹¹ starting in 2020, which causes epidemic patterns to deviate from their original stable
¹¹² annual cycle for a short period of time and eventually come back (Figure 2A). To
¹¹³ measure the resilience of this system empirically, we first need to be able to measure
¹¹⁴ the distance from its pre-pandemic attractor, which is defined as a set of points
¹¹⁵ in state space or phase plane that the system is pulled towards [19]. There are
¹¹⁶ many ways we can measure the distance from the attractor, but for illustrative
¹¹⁷ purposes, we choose one of the most parsimonious approaches: that is, we look at
¹¹⁸ how the susceptible (S) and infected (I) populations change over time and measure
¹¹⁹ the Euclidean distance on the SI phase plane, using the counterfactual unperturbed
¹²⁰ phase plane as a reference (Figure 2B; Materials and Methods). In this simple case,
¹²¹ the locally estimated scatterplot smoothing (LOESS) fit indicates that the distance
¹²² from the attractor decreases exponentially (linearly on a log scale) on average (Figure
¹²³ 2C). Furthermore, the overall rate of return approximates the intrinsic resilience of
¹²⁴ the seasonally unforced system (Figure 2C).

¹²⁵ Resilience of a single-strain system under a long-term perturbation.

¹²⁶ Alternatively, pandemic perturbations can have a lasting impact on the ~~pathogen~~
¹²⁷ ~~dynamics; as forces driving pathogen dynamics through a long-term reduction in~~
¹²⁸ ~~transmission or permanent change in immunity.~~ As an example, we consider a
¹²⁹ scenario in which a 10% reduction in transmission persists even after the major
¹³⁰ pandemic perturbations are lifted (Figure 2D–F). In such cases~~in practice~~, we can-
¹³¹ not know whether the pathogen will return to its original cycle or a different cycle
¹³² until many years have passed, and we cannot measure the distance to the new un-

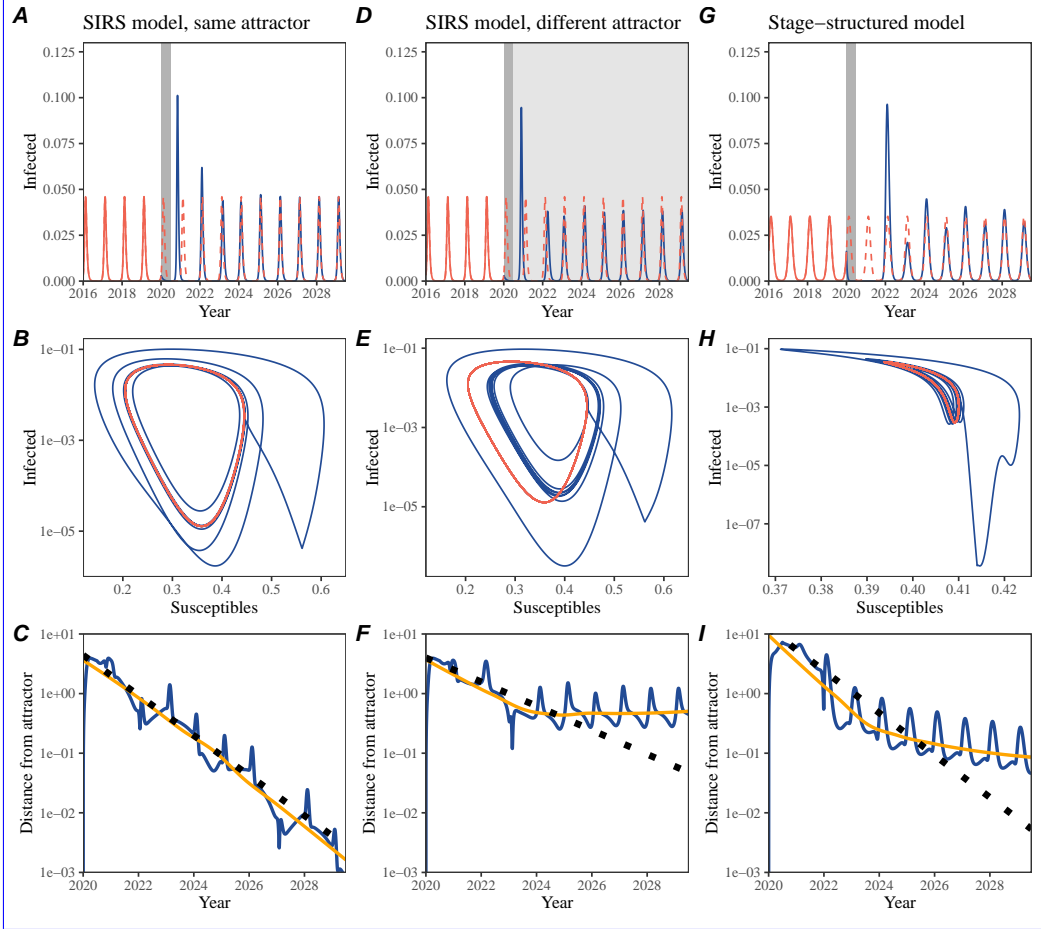


Figure 2: A simple method to measure pathogen resilience following pandemic perturbations across different scenarios. (A, D, G) Simulated epidemic trajectories across various models. Red and blue solid lines represent epidemic dynamics before and after pandemic perturbations are introduced, respectively. Red dashed lines represent counterfactual epidemic dynamics in the absence of perturbations. Gray regions indicate the duration of perturbations with the dark gray region representing a 50% transmission reduction and the light gray region representing a 10% transmission reduction. (B, E, H) Phase plane representation of the time series in panels A, D, and G alongside the corresponding susceptible host dynamics. Red and blue solid lines represent epidemic trajectories on an SI phase plane before and after perturbations are introduced, respectively. (C, F, I) Changes in logged distance from the attractor over time on a log scale. Blue lines represent the logged distance from the attractor. Orange lines represent the locally estimated scatterplot smoothing (LOESS) fits to the logged distance from the attractor. Dotted lines show the intrinsic resilience of the seasonally unforced system.

known attractor that the system might eventually approach. Nonetheless, we can still measure the distance from the pre-pandemic attractor and ask how the distance changes over time (Figure 2E). The LOESS fit suggests that the distance from the pre-pandemic attractor will initially decrease exponentially on average (equivalently, linearly on a log scale) and eventually plateau (Figure 2F). Here, a permanent 10% reduction in transmission rate slows the system, which causes the distance from the pre-pandemic attractor initially to decrease at a slower rate (Figure 2F) than it would have otherwise (Figure 2C) before plateauing at a fixed distance between the two attractors. This example shows that resilience is not necessarily an intrinsic property of a specific pathogen. Instead, pathogen resilience is a property of a specific attractor that a host-pathogen system approaches, which depends on both pathogen and host characteristics.

Resilience of a single-strain system with long-term transients. Finally, transient phenomena can further complicate the picture (Figure 2G–I). For example, a stage-structured model, which accounts for reduction in secondary susceptibility, initially exhibits a stable annual cycle, but perturbations from a 10% reduction in transmission for 6 months cause the epidemic to shift to biennial cycles (Figure 2G). The system eventually approaches the original pre-pandemic attractor (Figure 2H), suggesting that this biennial cycle is a transient **phenomenon**. The LOESS fit indicates that the distance from the attractor initially decreases exponentially at a rate that is consistent with the intrinsic resilience of the seasonally unforced stage-structured system, but the ~~rate of decrease decelerates approach to the attractor slows down~~ with the damped oscillations (Figure 2I). This behavior is also referred to as a ghost attractor, which causes long transient dynamics and slow transitions [20]. Strong seasonal forcing in transmission can also lead to transient phenomena for a simple SIRS model, causing a slow return to pre-perturbation dynamics (Supplementary Figure S1).

Resilience of a two-strain system. This empirical approach allows us to measure the resilience of a two-strain host-pathogen system as well even when we have incomplete observation of the infection dynamics. Simulations from a simple two-strain competition system illustrate that separate analyses of individual strain dynamics (e.g., RSV A vs B) and a joint analysis of total infections (e.g., total RSV infections) yield identical resilience estimates (Supplementary Figure S2, 3). This is expected because ~~eigenvalues determine the dynamics of two strains (or two pathogens) around the attractor in a coupled system are described by the same set of eigenvalues and eigenvectors~~ the entire system around the equilibrium, meaning that both strains should exhibit identical rates of ~~returns return~~ following a perturbation. Analogous to a single single-strain system, strong seasonal forcing in transmission can cause the two-strain system to slow down through transient phenomena (Supplementary Figure S4).

These observations ~~indicate three possibilities~~ yield three insights. First, we can directly estimate the empirical resilience of a host-pathogen system by measuring the rate at which the system approaches an attractor, provided that we have a

way to quantify the distance from the attractor—as we discuss later, the attractor of a system can be reconstructed from data from mathematical theory without making assumptions about the underlying model. The empirical approach to estimating pathogen resilience is particularly convenient because it does not require us to know the true underlying model; estimating the intrinsic resilience from fitting misspecified models can lead to biased estimates (Supplementary Figure S5). Second, resilience estimates allow us to make phenomenological predictions about the dynamics of a host-pathogen system following a perturbation. Assuming that an attractor has not changed and the distance from the attractor will decrease exponentially over time, we can obtain a ballpark estimate for estimate when the system will reach an attractor; this prediction necessarily assumes that there won't be permanent changes in pathogen dynamics (Figure 2F) or a long-term transient phenomenon (Figure 2I). Finally, a change in the rate of an exponential decrease in the distance from the attractor can (exponential) rate of approach provide information about whether the system has reached an alternative attractor, or a ghost attractor, that is different from the original, pre-pandemic attractor. These alternative attractors may reflect continued perturbations from permanent changes in transmission patterns as well as changes in immune landscapes. There will be periods of time when it is difficult to tell whether pathogen dynamics are still diverging from its original attractor or have begun to converge to an attractor; now the original attractor due to a long-term perturbation, or have entered the basin of attraction of a new attractor. Now that several years have passed since major interventions have been lifted, we expect many respiratory pathogens to may have had sufficient time to begin returning to their post-intervention attractors. attractors—empirical comparisons between current cases and pre-pandemic cases are consistent with this hypothesis (Figure 1). With recent data, we can start to evaluate whether we see early signs of convergence to the former attractor or a new one.

Inferring pathogen resilience from real data

Based on these observationspatterns, we now lay out our approach to estimating pathogen resilience from real data (Figure 3). We then test first tested this approach against simulations and apply applied it to real data. Specifically, we analyzed case time series of respiratory pathogens from four countries: Canada, Hong Kong, Korea, and the US.

So far, we have focused on simple examples that assume a constant transmission reduction during the pandemic. However, in practice, the impact of pandemic perturbations on pathogen transmission is was likely more complex (Figure 3A), reflecting introduction and relaxation of various intervention strategies. In some cases, strong perturbations can even lead to a local fadeout likely caused local fadeouts, requiring immigration/importation from another location for epidemic re-emergence. These complexities can rebound. Such complexities could lead to longer delays between

216 the introduction of pandemic perturbations and pathogen ~~re-emergence-rebound~~ as
217 well as temporal variation in outbreak sizes (Figure 3B); in this example, contin-
218 ued transmission reduction from interventions limits the size of the first outbreak in
219 2021 following the ~~emergence~~rebound, allowing for a larger outbreak in 2022 when
220 interventions are further relaxed.

221 Previously, we relied on the dynamics of susceptible and infected hosts to com-
222 pute the distance from the attractor (Figure 2), but information on susceptible hosts
223 is rarely available in practice. In addition, uncertainties in case counts due to ob-
224 servation error~~as well as~~, strain evolution, and multiannual cycles in the observed
225 epidemic dynamics (e.g., adenovirus circulation patterns in Hong Kong and Ko-
226 rea) add challenges to defining pre-pandemic attractors, which limits our ability to
227 measure the distance from the attractor. To address these challenges, we can re-
228 construct an empirical attractor by utilizing Takens' theorem [17], which states that
229 an attractor of a nonlinear multidimensional system can be mapped onto a delayed
230 embedding (Materials and Methods). For example, we can use delayed logged values
231 of pre-pandemic cases $C(t)$ (Figure 3C) to reconstruct the attractor:

$$\langle \log(C(t) + 1), \log(C(t - \tau) + 1), \dots, \log(C(t - (M - 1)\tau) + 1) \rangle, \quad (1)$$

232 where the delay τ and embedding dimension M are determined based on autocorre-
233 lations and false nearest neighbors, respectively [21, 22]. This allows us to define the
234 pre-pandemic attractor as a points on an M dimensional space. We can then apply
235 the same delay and embedding dimensions to the entire time series to determine
236 the position ~~on-a-in~~ multi-dimensional state space (Figure 3D), which allows us to
237 measure the nearest neighbor distance between the current state of the system and
238 the empirical pre-pandemic attractor (Figure 3E). Specifically, the nearest neighbor
239 distance is calculated by computing the distance between the current position on
240 the M dimensional space and all points in the empirical attractor set and taking
241 the minimum value. In theory, we can now quantify how fast this distance decreases
242 by fitting a linear regression on a log scale, where the slope of the linear regression
243 ~~corresponds to pathogen resilience~~ empirically measures pathogen resilience with a
244 steeper slope corresponding to a higher resilience estimate (Figure 3E). However,
245 resulting estimates of pathogen resilience can be sensitive to choices about embedding
246 delays and dimensions; ~~for~~. For example, using longer delays and higher dimen-

247 sions tends to smooth out temporal variations in the distance from the attractor
248 (Supplementary Figure S6).

249 Complex changes in the distance from the attractor suggest that estimating
250 pathogen resilience from linear regression will be particularly sensitive to our choice
251 of fitting windows for the regression (Figure 3E). Therefore, before we tried estimat-
252 ing resilience from real data, we explored an automated window selection criterion
253 for linear regression and ~~test~~tested it against randomized, stochastic simulations
254 across a ~~wide~~ range of realistic pandemic perturbation shapes; ~~in~~. In doing so, we
255 also explored optimal choices for embedding dimensions and evaluated our choices
256 ~~for~~of fitting window parameters and embedding dimensions by quantifying corre-

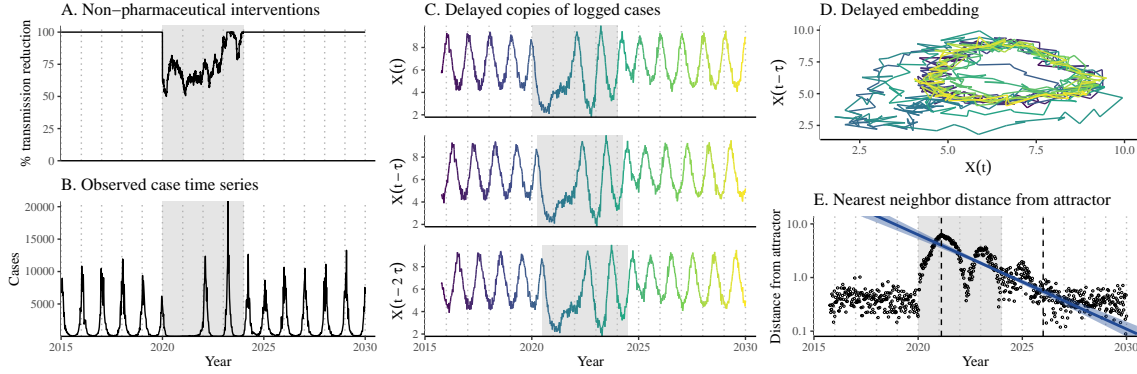


Figure 3: **A schematic diagram explaining the inference of pathogen resilience from synthetic data.** (A) A realistic example of simulated pandemic perturbations, represented by a relative reduction in transmission. (B) The impact of the synthetic pandemic perturbation on epidemic dynamics simulated using a SIRS model with demographic stochasticity. (C) Generating delayed copies of the logged time series allows us to obtain an embedding. (D) Two dimensional representation of an embedding. (E) Delayed embedding allows us to calculate the nearest neighbor distance from the empirical attractor, which is determined based on the pre-pandemic time series. Blue lines and dashed regions represent the linear regression fit and the associated 95% confidence interval. This distance time series can be used to infer pathogen resilience after choosing an appropriate window for linear regression. For illustration purposes, an arbitrary fitting window was chosen.

257 lation coefficients between the estimated resilience and the intrinsic resilience of a
 258 seasonally unforced system (Materials and Methods). Overall, we ~~find~~found large
 259 variation in estimation performances with correlation coefficient ranging from 0.21
 260 to 0.61 (Supplementary Figure S7). In almost all cases, the automated window
 261 selection approach outperformed a naive approach~~that uses the entire time series,~~
 262 ~~starting from~~, which performs regression between the peak distance and current
 263 distance (Supplementary Figure S7).

264 Based on the best performing window selection criteria and embedding dimen-
 265 sion, we applied this approach to pathogen surveillance data presented in Figure
 266 1 (Materials and Methods). For each time series, we applied Takens' theorem in-
 267 dependently to reconstruct the empirical attractor and obtained the corresponding
 268 time series of distances from attractors (Supplementary Figure S8). Then, we ~~use~~
 269 used the automated window selection criterion to fit a linear regression and ~~estimate~~
 270 estimated the empirical resilience for each pathogen in each country (Supplementary
 271 Figure S8); the window selection criterion gave poor regression window for three
 272 cases (norovirus in Hong Kong and Korea and ~~Rhinovirus~~rhinovirus/~~Enterovirus~~
 273 enterovirus in the US), leading to unrealistically low resilience estimates, and so we
 274 used ad-hoc regression windows instead (Supplementary Figure S9; Materials and
 275 Methods).

276 For all pathogens we ~~consider~~considered, resilience estimates ~~fall~~fell between
277 0.4/year and 1.8/year (Figure 4A). We ~~estimate~~estimated the mean resilience of
278 common respiratory pathogens to be 0.99/year (95% CI: 0.81/year–1.18/year). **As**
279 ~~a~~For reference, this is \approx 7.5 times higher than the intrinsic resilience of pre-
280 vaccination measles in England and Wales (\approx 0.13/year). Finally, resilience esti-
281 mates for norovirus~~are~~are, a *gastrointestinal pathogen*, ~~were~~were comparable to those of
282 common respiratory pathogens: 1.44/year (95% CI: 1.01/year–1.87/year) for Hong
283 Kong and 1.07/year (95% CI: 0.86/year–1.29/year) for Korea. Based on a simple
284 ANOVA test, we ~~do~~did not find significant differences in resilience estimates across
285 countries ($p = 0.25$) or pathogens ($p = 0.67$).

286 Using resilience estimates, we predicted when each pathogen would hypotheti-
287 cally return to their pre-pandemic dynamics, assuming no long-term change in the
288 attractor. Specifically, we ~~extend~~extended our linear regression fits to distance-
289 from-attractor time series and ask when the predicted regression line will cross a
290 threshold value; since we relied on nearest neighbor distances, pre-pandemic dis-
291 tances are always greater than zero (Figure 3E), meaning that we can use the mean
292 of pre-pandemic distances as our threshold.

293 We ~~predict~~predicted that a return to pre-pandemic cycles ~~has occurred or~~ would
294 be imminent for most pathogens (Figure 4B). In particular, we ~~predict~~predicted
295 that 12 out of 23 ~~pathogens~~pathogen-country pairs should have already returned
296 before the end of 2024. For almost all pathogens that ~~are~~were predicted to have
297 returned already, the observed epidemic dynamics ~~show~~showed clear convergence
298 towards their pre-pandemic seasonal averages, confirming our predictions (Figure
299 4C). However, there ~~are~~were a few exceptions, including norovirus in Hong Kong
300 and ~~Rhinovirus~~rhinovirus/Enterovirus~~enterovirus~~ in the US, where the observed
301 epidemic dynamics in 2024 exhibit clear deviation from their pre-pandemic seasonal
302 averages (Figure 4C; Figure S9). These observations suggest a possibility that some
303 common respiratory pathogens may have converged to different attractors or are still
304 exhibiting non-equilibrium dynamics. In contrast, pathogens that ~~are~~were predicted
305 to have not returned yet also ~~show~~showed clear differences from their pre-pandemic
306 seasonal averages; as many of these pathogens are predicted to return in 2025–2026,
307 we may be able to test these predictions in near future (Supplementary Figure S10).
308 Our reconstructions of distance time series and estimates of pathogen resilience and
309 expected return time ~~are~~were generally robust to choices of embedding dimensions
310 (Supplementary Figure S11–12).

311 Susceptible host dynamics explain variation in pathogen 312 resilience

313 So far, we ~~have~~have focused on quantifying pathogen resilience from the observed pat-
314 terns of pathogen re-emergence following pandemic perturbations. But what factors
315 determine how resilient a host-pathogen system is? ~~Here, we use~~To address this

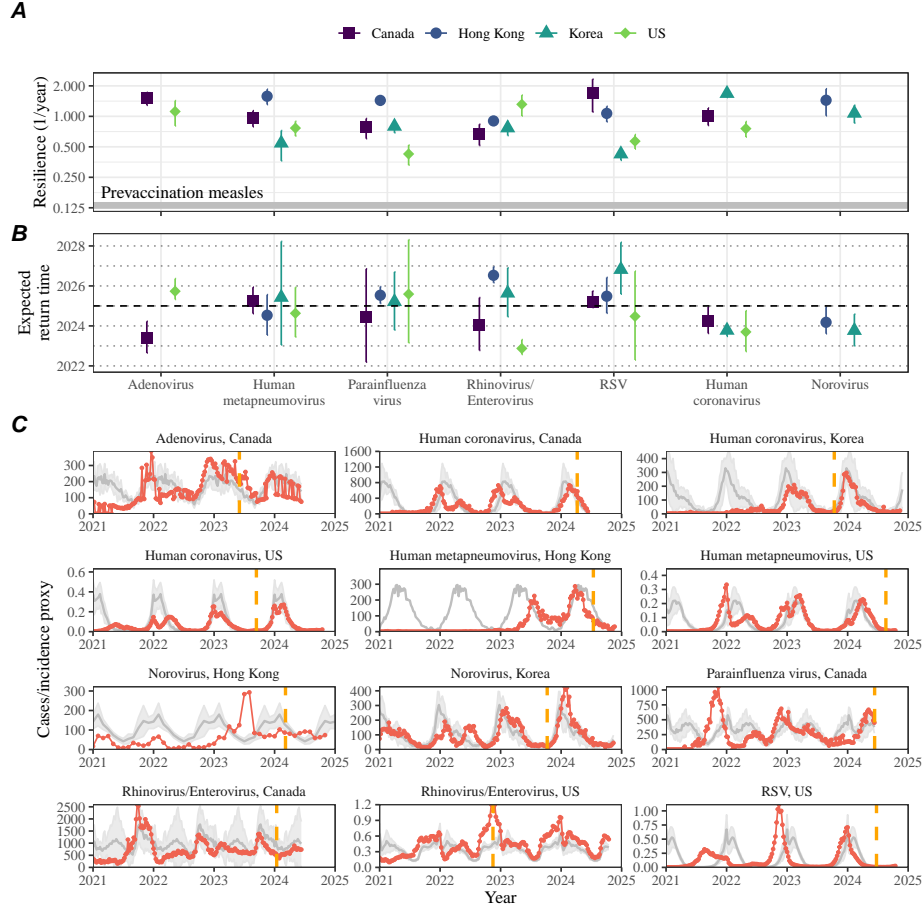


Figure 4: **Summary of resilience estimates and predictions for return time.** (A) Estimated pathogen resilience. The gray horizontal line represents the intrinsic resilience of pre-vaccination measles dynamics. (B) Predicted timing of when each pathogen will return to their pre-pandemic cycles. The dashed line in panel B indicates the end of 2024 (current observation time). Error bars represent 95% confidence intervals. (C) Observed dynamics for pathogen that are predicted to have returned before the end of 2024. Red points and lines represent data before 2020. Gray lines and shaded regions represent the mean seasonal patterns and corresponding 95% confidence intervals around the mean, previously shown in Figure 1. Orange vertical lines represent the predicted timing of return.

316 question, we used the SIRS model to show that explore how changes in susceptible
 317 host dynamics are the key determinants of affect pathogen resilience. To do so, we
 318 vary varied the basic reproduction number \mathcal{R}_0 , which represents the average number
 319 of secondary infections caused by a newly infected individual in a fully susceptible
 320 population, and the duration of immunity and eompute computed intrinsic resilience
 321 for each parameter.

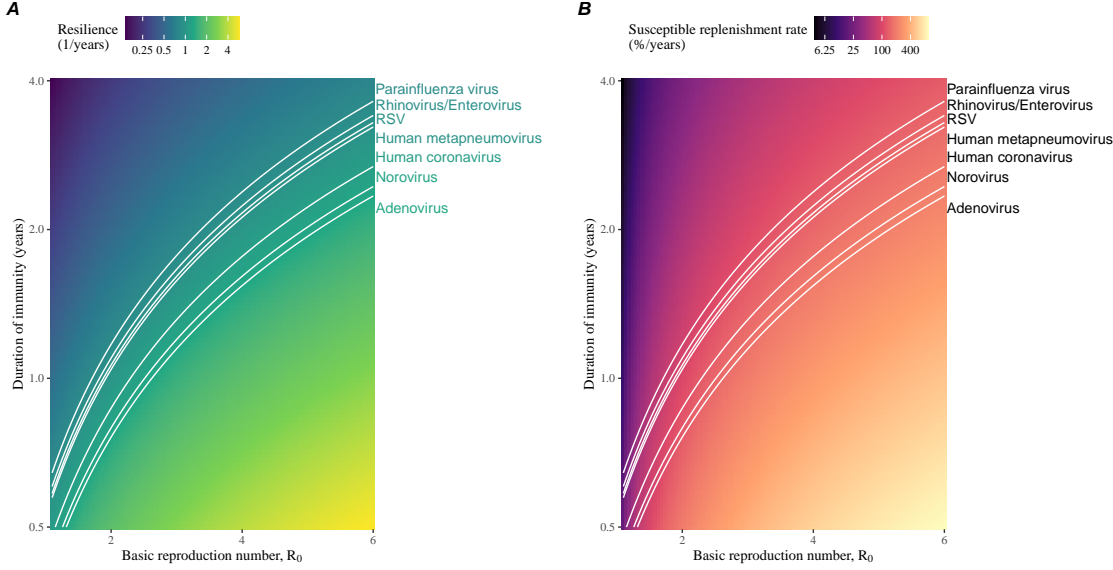


Figure 5: **Linking pathogen resilience to epidemiological parameters and susceptible host dynamics.** (A) The heat map represents intrinsic resilience as a function of the basic reproduction number R_0 and the duration of immunity. (B) The heat map represents per-capita susceptible replenishment rate as a function of the basic reproduction number R_0 and the duration of immunity. The standard SIRS model without seasonal forcing is used to compute intrinsic resilience and the per-capita susceptible replenishment rate. Lines correspond to a set of parameters that are consistent with mean resilience estimates for each pathogen. Pathogens are ranked based on their mean resilience estimates, averaged across different countries.

We find that an increase in R_0 and a decrease in the duration of immunity correspond to an increase in pathogen resilience (Figure 5A). These variations can be understood in terms of the susceptible host dynamics, where similarly, an increase in R_0 and a decrease in the duration of immunity corresponds to a faster per-capita susceptible replenishment rate causes the system to be more resilient (Figure 5B). This rate can be expressed as a rate of susceptible replenishment, which is defined as the ratio between absolute rate at which new susceptibles enter the population and the equilibrium number of susceptible individuals in the population, \bar{S} . Therefore, both S^* (Figure 5B). We note that a higher R_0 and shorter duration of immunity can drive a faster per-capita susceptible replenishment rate (Figure 5B), especially because higher R_0 leads to lower \bar{S} by decreasing the susceptible proportion at equilibrium, S^* . For a simple SIR model that assumes a life-long immunity, we can show analytically that pathogen resilience is proportional to the per-capita rate of susceptible replenishment (Materials and Methods). Overall, these observations suggest that a faster per-capita susceptible replenishment rate causes

337 the system to be more resilient.

338 We can also rank different pathogens based on By taking the average values of
339 empirical resilience computed previously, which allows us to determine values for
340 each pathogen, we were able to map each pathogen onto a set of parameters of the
341 SIRS model that are consistent with the estimated resilience corresponding resilience
342 estimates (Figure 5A). Across all pathogens we consider, except for boeavirus and
343 norovirus, we estimate considered, we estimated that the average duration of immu-
344 nity is likely to be short (< 4 years) across a plausible range of \mathcal{R}_0 (< 6). These
345 rankings further allow us to map each pathogen onto a set of SIRS parameters
346 that are consistent with its empirical resilience (Figure 5A) and We were also able
347 to obtain a plausible range of susceptible replenishment rates for each pathogen
348 (Figure 5B). However, we note that there is no one-to-one correspondence between
349 susceptible replenishment rates and pathogen resilience, leading to a wide, but there
350 was a large uncertainty in the estimates for susceptible replenishment rates (Figure
351 5B) due to a lack of one-to-one correspondence between susceptible replenishment
352 rates and pathogen resilience.

353 Pathogen resilience determines sensitivity to stochastic perturbations

354

355 Beyond the Even in the absence of major pandemic perturbations, we expect host-
356 pathogen systems are expected to experience continued perturbations of varying de-
357 grees from changes in epidemiological conditions, such as human behavior, climate,
358 and viral evolution. These perturbations can also arise from demographic stochas-
359 ticity, which is inherent to any ecological systems. Here, we use used a seasonally
360 unforced SIRS model with birth/death constant birth and death rates to explore
361 how resilience of a host-pathogen system determines the sensitivity to perturbations
362 caused by demographic stochasticity (Materials and Methods).

363 We find found that resilience of a host-pathogen system determines the amount
364 of deviation from the deterministic trajectory caused by demographic stochasticity,
365 with less resilient systems experiencing larger deviations (Figure 6). Notably, less
366 resilience systems also exhibit resilient systems also exhibited slower epidemic cycles ;
367 the (Figure 6A–C). The periodicity of this epidemic cycle matches matched those pre-
368 dicted by the intrinsic periodicity of the system (Supplementary Figure S13) . These
369 conclusions are where the intrinsic resilience of the system is inversely proportional
370 to its intrinsic periodicity (Supplementary Figure S14). However, we note that
371 the interplay between seasonal transmission and intrinsic periodicity can also lead
372 to complex cycles, as illustrated by a recent analysis of *Mycoplasma pneumoniae*
373 dynamics [23].

374 We also note that the intrinsic resilience is not the sole determinant for how
375 sensitive the system is to stochastic perturbations. For example, the population
376 size and average duration of infection also affect the amount of deviation from

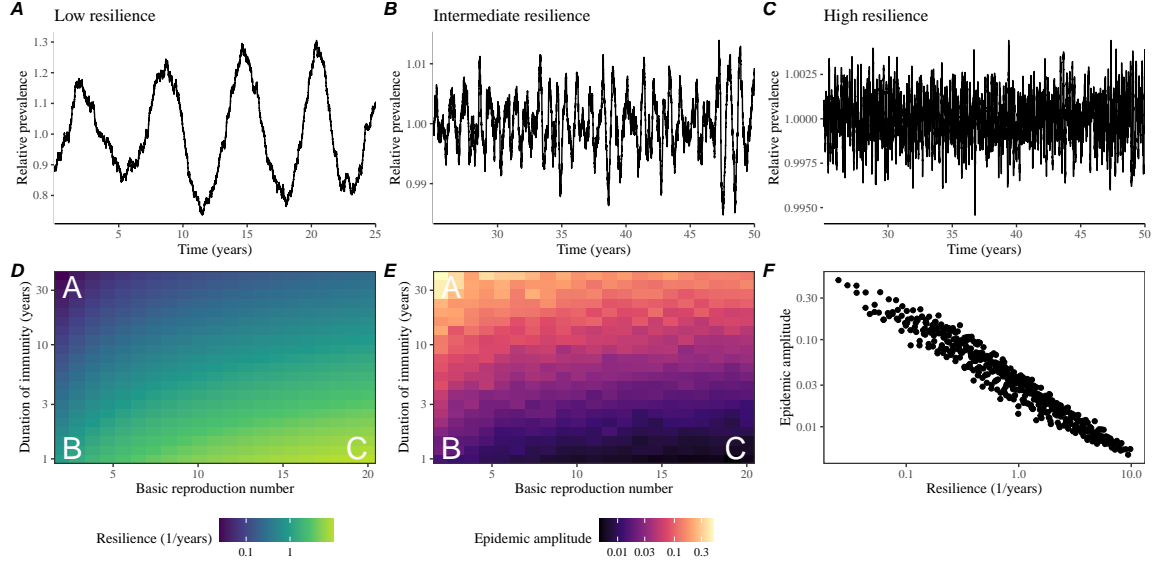


Figure 6: Linking resilience of a host-pathogen system to its sensitivity to stochastic perturbations. (A–C) Epidemic trajectories of a stochastic SIRS model across three different resilience values: low, intermediate, and high. The relative prevalence was calculated by dividing infection prevalence by its mean value. (D) **The heat map represents the intrinsic** **Intrinsic** resilience of a system as a function of the basic reproduction number \mathcal{R}_0 and the duration of immunity. (E) **The heat map represents the epidemic** **Epidemic** amplitude as a function of the basic reproduction number \mathcal{R}_0 and the duration of immunity. The epidemic amplitude corresponds to $(\max I - \min I)/(2\bar{I})$, where \bar{I} represents the mean prevalence. **Labels A–C in panels D and E correspond to scenarios shown in panels A–C.** (F) The relationship between pathogen resilience and epidemic amplitude.

377 the deterministic trajectory caused by demographic stochasticity, even though these
 378 quantities have little to no impact on the intrinsic resilience (Supplementary Figure
 379 S15). These conclusions were robust for the seasonally forced SIRS model (Supple-
 380 mentary Figure S14), S16).

381 Discussion

382 **The pandemic interventions have COVID-19 pandemic interventions** caused major
 383 disruptions to circulation patterns of both respiratory and non-respiratory pathogens,
 384 adding challenges to predicting their future dynamics [1, 2, 3, 4]. However, these
 385 perturbations offer large-scale natural experiments for understanding how different
 386 pathogens respond to perturbations. In this study, we showed that pathogen re-
 387 emergence patterns following pandemic perturbations can be characterized through

388 the lens of ecological resilience and presented a new method for estimating pathogen
389 resilience from time series data. We showed that variation in pathogen resilience
390 can be explained by the differences in susceptible host dynamics, where faster re-
391 replenishment of the susceptible pool corresponds to a more resilient host-pathogen
392 system. Finally, we showed that pathogen resilience also determines the sensitivity
393 to stochastic perturbations.

394 We analyzed case time series of common respiratory infections and norovirus in-
395 fections from Canada, Hong Kong, Korea, and the US to estimate their resilience.
396 Overall, we estimated the resilience of these pathogens to range from 0.4/year to
397 1.8/year, which is 3–14 times more resilient than prevaccination measles. These
398 Consistent with other epidemiological evidence [24, 25, 26, 27], these resilience es-
399 timates indicate that common respiratory pathogens and norovirus likely exhibit
400 faster susceptible replenishment and are therefore more persistent, indicating poten-
401 tial challenges in controlling these pathogens.

402 Based on our resilience estimates, we made phenomenological predictions about
403 when each pathogen will return to their endemic cycles. For the most part, we
404 accurately predicted which pathogens should have already returned before the end
405 of 2024. However, there were fewtwo main exceptions (i.e., norovirus in Hong
406 Kong and rhinovirus/enterovirus in the US), suggesting a possibility that these
407 may have converged to different endemic cycles compared to their pre-pandemic
408 epidemic patternsthat these pathogens may be converging to new endemic cycles
409 or experiencing long-term transient behavior. These changes may reflect changes in
410 surveillance or actual shift in the dynamics, caused by permanent changes in be-
411 havior or population-level immunity. While it may seem unlikely that permanent
412 changes in behavior would only affect a few pathogens and not others, we cannot
413 rule out this possibility given heterogeneity in the age of infection across different
414 respiratory pathogensdifferences in the observed mean age of infections and therefore
415 the differences in age groups that primarily drive transmission [28, 29]. Differences
416 in the mode of transmission between respiratory vs gastrointestinal pathogens may
417 also contribute to the differences in responses to pandemic perturbations. However,
418 it is unclear why norovirus dynamics in Korea seemed to have returned, whereas
419 those in Hong Kong have not.

420 For almost half of the pathogens we considered, we predicted that their return
421 to original epidemic patterns is imminent. We will need a few more years of data
422 to test whether these pathogens will eventually return to their original dynamics or
423 eventually converge to a different attractor. We also cannot rule out the possibility
424 that some pathogens may exhibit long-term transient behaviors following pandemic
425 perturbations. Overall, these observations echo earlier studies that highlighted the
426 long-lasting impact of pandemic perturbations [8, 30, 31, 4][8, 30, 31, 4, 23].

427 We showed that susceptible host dynamics shape pathogen resilience, where faster
428 replenishment of the susceptible population causes the pathogen to be more resilient.
429 For simplicity, we focusfocused on waning immunity and birth as the main drivers
430 of the susceptible host dynamics but other mechanisms can also contribute to the

431 replenishment of the susceptible population. In particular, pathogen evolution, es-
432 pecially the emergence of antigenically novel strains, can cause effective waning of
433 immunity in the population; therefore, we hypothesize that ~~faster rates~~ ~~the rate~~
434 of antigenic evolution ~~can also cause a pathogen to be more resilient~~ ~~is likely a key~~
435 ~~feature of pathogen resilience~~. Future studies should explore the relationship between
436 the rate of evolution and resilience for antigenically evolving pathogens. ~~This result~~
437 ~~also highlights the importance of detailed measurements of changes in the susceptible~~
438 ~~population through serological assays for understanding pathogen dynamics [32]~~.

439 Quantifying pathogen resilience also offers novel approaches to validating population-
440 level epidemiological models. So far, most ~~of~~ model validation in infectious disease
441 ecology is based on the ability of a model to reproduce the observed epidemic dy-
442 namics and to predict future dynamics [33, 34, 26, 35, 36]. However, many models
443 can perform similarly under these criteria. For example, two major RSV models have
444 been proposed to explain biennial epidemic patterns: (1) a stage- and age-structured
445 model that allows disease severity to vary with number of past infections and age
446 of infection [26] and (2) a pathogen-interaction model that accounts for cross im-
447 munity between RSV and human ~~metapnuemovirus~~ ~~metapneumovirus~~ [34]. Since
448 both models can accurately reproduce the observed epidemic patterns, standard cri-
449 teria for model validation do not allow us to distinguish between these two models
450 from population-level data alone. Instead, it would be possible to measure the em-
451 pirical resilience of each model by simulating various perturbations and ~~eompare~~
452 ~~them~~ ~~comparing the simulations~~ to estimates of empirical resilience from data, using
453 pandemic perturbations as ~~an opportunity~~ ~~a reference~~.

454 There are several limitations to our work. First, we did not extensively explore
455 other approaches to reconstructing the attractor. Recent studies showed that more
456 sophisticated approaches, such as using non-uniform embedding, can provide more
457 robust reconstruction for noisy data [22]. In the context of causal inference, choices
458 about embedding can have major impact on the resulting inference [37]. Our re-
459 silience estimates are likely overly confident given a lack of uncertainties in attractor
460 reconstruction as well as the simplicity of our statistical framework. Nonetheless,
461 as illustrated in our sensitivity analyses, inferences about pathogen resilience in our
462 SIRS model appear to be robust to decisions about embedding lags and dimensions—
463 this is because tracking the rate at which the system approaches the attractor is
464 likely a much simpler problem than making inferences about causal directionality.
465 Short pre-pandemic time series also limit our ability to accurately reconstruct the
466 attractor and contribute to the crudeness of our resilience estimates; although this
467 is less likely a problem for respiratory pathogens that are strongly annual, our at-
468 tractor reconstruction may be inaccurate for those exhibiting multi-annual cycles,
469 such as adenovirus in Hong Kong and Korea. ~~Our framework also do not allow us~~
470 ~~to distinguish whether a system has settled to a new attractor or is experiencing~~
471 ~~long-term transient behavior~~. Uncertainties in pathogen dynamics due to changes
472 in testing patterns further contribute to the ~~eurdness~~ ~~crudeness~~ of our resilience
473 estimates.

474 While attractor reconstruction methods allow us to make model-free inferences
475 of pathogen resilience, it does not allow us to tease apart how different mechanisms
476 contribute to the resilience a host-pathogen system. Using the simple SIRS model,
477 we illustrated that susceptible host dynamics are key determinants for pathogen
478 resilience, but we also found that there isn't a one-to-one correspondence between
479 per capita replenishment rate of the susceptible population and pathogen resilience
480 estimates. Future studies should explore using mechanistic models to explain heterogeneity
481 in resilience estimates across different pathogens.

482 Finally, our simulation-based analyses primarily focused on single-strain systems
483 but real-world pathogens can interact with other pathogens, which can result in
484 complex dynamics [38, 39]. To address this limitation, we considered a simple
485 two-strain competition system with cross immunity and showed that the resilience
486 of a coupled system can be measured by studying the dynamics of either strains.
487 However, this conclusion likely depend on the strength of strain interaction as well as
488 the underlying details of the model. For example, ecological interference between two
489 unrelated pathogens [38] will likely generate weaker coupling than cross immunity
490 between related pathogens; in the former case, we do not necessarily expect two
491 unrelated pathogens to have same resilience despite their ecological interference.
492 Some pathogen strains can also exhibit positive interactions where infection by
493 one strain can lead to an increased transmission of another competing strain. For
494 example, previous studies showed that an increased dengue transmission through
495 antibody-dependent enhancement can permit coexistence and persistence of competing
496 strains [40]; based on these observations, we tentatively hypothesize that positive
497 interactions such as antibody-dependent enhancement may increase the resilience
498 of a system. Future studies should explore how different mechanisms of pathogen
499 interactions contribute to the resilience of each competing pathogen as well as the
500 entire system. Despite these limitations, our study illustrates that quantifying pathogen
501 resilience can provide novel insights into pathogen dynamics. Furthermore, our
502 qualitative prediction that common respiratory pathogens are more resilient than prevac-
503 cination measles is also likely to be robust, given how rapid rapidly many respiratory
504 pathogens returned to their original cycles following pandemic perturbations.

505 Predicting the impact of anthropogenic changes on infectious disease dynamics
506 is a fundamental aim of infectious disease research in a rapidly changing world. Our
507 study illustrates that how a host-pathogen system responds to both small and large
508 perturbations is largely predictable through the lens of ecological resilience. In par-
509 ticular, quantifying the resilience of a host-pathogen system offers a unique insight
510 into questions about endemic pathogens' responses to pandemic perturbations, in-
511 cluding whether some pathogens will exhibit long-lasting impact from the pandemic
512 perturbation or not. More broadly, a detailed understanding of the determinants of
513 pathogen resilience can provide deeper understanding of pathogen persistence.

514 **Materials and Methods**

515 **Data**

516 We gathered time series on respiratory infections from Canada, Hong Kong, Korea,
517 and United States (US). As a reference, we also included time series data on norovirus
518 infections ~~for available countries when available~~. In contrast to respiratory pathogens,
519 we ~~expect hypothesized~~ gastrointestinal viruses, such as norovirus, to be differently
520 affected by pandemic perturbations.

521 Weekly time series of respiratory infection cases in Canada ~~comes came~~ from a
522 publicly available website by the Respiratory Virus Detection Surveillance System,
523 which ~~collect collects~~ data from select laboratories across Canada [41]. Weekly time
524 series of respiratory infection cases in Hong Kong ~~comes came~~ from a publicly avail-
525 able website by the Centre for Health Protection, Department of Health [42, 43].
526 Weekly time series of acute respiratory infection cases in Korea ~~comes came~~ from a
527 publicly available website by the Korea Disease Control and Prevention Agency [44].
528 Finally, weekly time series of respiratory infection cases in the US were obtained from
529 the Centers for Disease Control and Prevention, National Respiratory and Enteric
530 Virus ~~Surveillance~~ Surveillance System. Time series on number of tests were also
531 available in Canada, Hong Kong, and the US, but not in Korea.

532 **Data processing**

533 For all time series, we rounded every year to 52 weeks by taking the average number
534 of cases and tests between the 52nd and 53rd week. We also ~~rescale rescaled~~ all time
535 series to account for changes in testing patterns, which ~~are were~~ then used for the
536 actual analysis.

537 For Canada, an increase in testing was observed from 2013 to 2024 (Supplemen-
538 tary Figure ~~S15~~S17). To account for this increase, we calculated a 2 year moving
539 average for the number of tests for each pathogen, which we used as a proxy for test-
540 ing effort. Then, we divided the smoothed testing patterns by the smoothed value
541 at the final week such that the testing effort has a maximum of 1. We then divided
542 weekly cases by the testing effort to obtain a scaled case time series. A similar ap-
543 proach was used earlier for an analysis of RSV time series in the US to account for
544 changes in testing patterns [26].

545 For Hong Kong, we ~~also~~ applied the same scaling procedure to the time series
546 as we did for Canada. In this case, we only adjusted for testing efforts up to the
547 end of 2019 because there was a major reduction in testing for common respiratory
548 pathogens ~~since between~~ 2020 and 2023 (Supplementary Figure ~~S16~~S18).

549 For Korea, while we did not have information on testing, the reported number of
550 respiratory infections consistently increased from 2013 to the end of 2019, which we
551 interpreted as changes in testing patterns (Supplementary Figure ~~S17~~S19). Since we
552 did not have testing numbers, we used the weekly sum of all acute respiratory viral

553 infection cases as a proxy for testing, which were further smoothed with moving
554 ~~averaged~~average and scaled to have a maximum of 1. For Korea, we also only
555 adjusted for testing efforts up to the end of 2019.

556 In the US, there has been a large increase in testing ~~against~~for some respiratory
557 pathogens, especially RSV, which could not be corrected ~~for through by~~ simple scal-
558 ing (Supplementary Figure S18S20). Instead, we derived an incidence proxy by mul-
559 tiplying the test positivity with influenza-like illness positivity, which was taken from
560 <https://gis.cdc.gov/grasp/fluview/fluportaldashboard.html>. This method
561 of estimating an incidence proxy has been recently applied in the analysis of seasonal
562 coronaviruses [7] and *Mycoplasma pneumoniae* infections [4]. Detailed assumptions
563 and justifications are provided in [45].

564 Data summary

565 To make qualitative comparisons between pre- and post-perturbation dynamics of
566 respiratory pathogen circulation patterns, we calculated the mean seasonal patterns
567 using time series of either rescaled cases or incidence proxy estimates before 2020. We
568 did so by taking the mean value in each week across all years before 2020. Confidence
569 intervals around the means were calculated using a simple t test.

570 Estimating pathogen resilience

571 In order to measure pathogen resilience from surveillance data, we first reconstructed
572 the empirical pre-pandemic attractor of the system using Takens' embedding theorem
573 [17]. Specifically, for a given pathogen, we took the pre-pandemic (before 2020) case
574 time series $C(t)$ and ~~reconstruct~~reconstructed the attractor using delayed embedding
575 with a uniform delay of τ and dimension M :

$$X_{\tau,m}(t) = \langle \log(C(t) + 1), \log(C(t - \tau) + 1), \dots, \log(C(t - (M - 1)\tau) + 1) \rangle. \quad (2)$$

576 Here, the delay τ was determined by calculating the autocorrelation of the logged
577 pre-pandemic time series and asking when the autocorrelation crosses 0 for the first
578 time [22]; a typical delay for ~~for~~ an annual outbreak is around 13 weeks.

579 Then, for a given delay τ , we determined the embedding dimension M using the
580 false nearest neighbors approach [21, 22]. To do so, we started with an embedding
581 dimension e and ~~construct~~constructed a set of points $A_{\tau,e} = \{X_{\tau,e}(t) | t < 2020\}$.
582 Then, for each point $X_{\tau,e}(t)$, we determined the nearest neighbor from the set $A_{\tau,e}$,
583 which we denote $X_{\tau,e}(t_{nn})$ for $t \neq t_{nn}$. Then, if the distance between these two
584 points ~~on in the~~ $e + 1$ dimension, $D_{\tau,e+1}(t) = \|X_{\tau,e+1}(t_{nn}) - X_{\tau,e+1}(t)\|_2$, is larger
585 than their distance ~~on in the~~ e dimension, $D_{\tau,e}(t) = \|X_{\tau,e}(t_{nn}) - X_{\tau,e}(t)\|_2$, these two
586 points are deemed to be false nearest neighbors; specifically, we used a threshold
587 R for the ratio between two distances $D_{\tau,e+1}(t)/D_{\tau,e}(t)$ to determine false nearest
588 neighbors. ~~The first embedding dimension e that does not have any false nearest~~
589 ~~neighbors corresponds to the embedding dimension M for a given pathogen-country~~

590 pair. For the main analysis, we used $R = 10$, which was chosen from a sensitivity
 591 analysis against simulated data (Supplementary Text). Once we determined the
 592 embedding lag τ and dimension M , we apply the embedding to the entire time series
 593 and calculate the nearest neighbor distance against the attractor $A_{\tau,M}$ to obtain a
 594 time series of distance from the attractor $D_{\tau,M}(t)$.

595 From a time series of distances from the attractor, we estimated pathogen re-
 596 silience by fitting a linear regression to an appropriate window. To automatically
 597 select ~~the fitting window~~fitting windows, we began by smoothing the distance time
 598 series using locally estimated scatterplot smoothing (LOESS) to obtain $\hat{D}_{\tau,M}(t)$,
 599 where the smoothing is performed on a log scale and exponentiated afterwards.
 600 This smoothing allowed us to find appropriate threshold values for selecting fitting
windows that are insensitive to errors in our estimates of distance from the attractor.
 601 Then, we determined threshold values (T_{start} and T_{end}) for the smoothed distances and
 602 choose the fitting window based on when $\hat{D}_{\tau,M}(t)$ crosses these threshold values for
 603 the first time. These thresholds were determined by first calculating the maximum
 604 distance,
 605

$$\max \hat{D} = \max \hat{D}_{\tau,M}(t), \quad (3)$$

606 and the mean pre-pandemic distance,

$$\hat{D}_{\text{mean}} = \frac{1}{N_{t < 2020}} \sum_{t < 2020} \hat{D}_{\tau,M}(t), \quad (4)$$

607 as a reference, and then dividing their ratios into K equal bins:~~as~~

$$T_{\text{start}} = \hat{D}_{\text{mean}} \times \left(\frac{\max \hat{D}}{\hat{D}_{\text{mean}}} \right)^{(K-a)/K}, \quad (5)$$

$$T_{\text{end}} = \hat{D}_{\text{mean}} \times \left(\frac{\max \hat{D}}{\hat{D}_{\text{mean}}} \right)^{a/K}, \quad (6)$$

608 where a represents the truncation threshold. This allows us to discard the initial
 609 period during which the distance increases (from the introduction of intervention
 610 measures) and the final period during which the distance plateaus (as the system
 611 reaches an attractor). The fitting window is determined based on when the smoothed
 612 distance $\hat{D}_{\tau,M}(t)$ crosses these threshold values for the first time; then, we fit a
 613 linear regression to logged (unsmoothed) distances $\log D_{\tau,M}(t)$ using that window.
 614 Alongside the threshold R for the false nearest neighbors approach, we tested optimal
 615 choices for K and a values using simulations (Supplementary Text). We used $K = 19$
 616 and $a = 2$ throughout the paper based on the simulation results.

617 Mathematical modeling

618 Throughout the paper, we use a series of mathematical models to illustrate the con-
 619 cept of pathogen resilience and to understand the determinants of pathogen resilience.

620 In general, the intrinsic resilience ~~for-of~~ a given system is given by the largest real
 621 part of the eigenvalues of the linearized system at endemic equilibrium. Here, we
 622 focus on the SIRS model with demography (birth and death) and present the details
 623 of other models in Supplementary Text. The SIRS (Susceptible-Infected-Recovered-
 624 Susceptible) model is the simplest model that allows for waning of immunity, where
 625 recovered (immune) individuals are assumed to become fully susceptible after an
 626 average of $1/\delta$ time period. The dynamics of the SIRS model is described by the
 627 following set of differential equations:

$$\frac{dS}{dt} = \mu - \beta(t)SI - \mu S + \delta R \quad (7)$$

$$\frac{dI}{dt} = \beta(t)SI - (\gamma + \mu)I \quad (8)$$

$$\frac{dR}{dt} = \gamma I - (\delta + \mu)R \quad (9)$$

628 where μ represents the birth ~~death rate and death rates~~, $\beta(t)$ represents the time-
 629 varying transmission rate, and γ represents the recovery rate. The basic reproduction
 630 number $\mathcal{R}_0(t) = \beta(t)/(\gamma + \mu)$ is defined as the average number of secondary infections
 631 that a single infected individual would cause in a fully susceptible population at time
 632 t and measures the intrinsic transmissibility of a pathogen.

633 When we ~~first~~ introduced the idea of pathogen resilience (Figure 2), we imposed
 634 sinusoidal changes to the transmission rate to account for seasonal transmission:
~~–~~

$$\beta(t) = b_1(1 + \theta \cos(2\pi(t - \phi)))\alpha(t), \quad (10)$$

635 where b_1 represents the baseline transmission rate, θ represents the seasonal am-
 636 plitude, and ϕ represents the seasonal offset term. Here, we also introduced an
 637 extra multiplicative term $\alpha(t)$ to account for the impact of pandemic perturbations,
 638 where $\alpha(t) < 1$ indicates transmission reduction. Figure 2A and 2B were gener-
 639 ated assuming $b_1 = 3 \times (365/7 + 1/50)/\text{years}$, $\theta = 0.2$, $\phi = 0$, $\mu = 1/50/\text{years}$,
 640 $\gamma = 365/7/\text{years}$, and $\delta = 1/2/\text{years}$. Specifically, $b_1 = 3 \times (365/7 + 1/50)/\text{years}$
 641 implies $\mathcal{R}_0 = 3$, where $(365/7 + 1/50)/\text{years}$ represent the rate of recovery. In Figure
 642 2A, we imposed a 50% transmission reduction for 6 months from 2020:

$$\alpha(t) = \begin{cases} 0.5 & 2020 \leq t < 2020.5 \\ 1 & \text{otherwise} \end{cases} \quad (11)$$

643 In Figure 2B, we imposed a 50% transmission reduction for 6 months from 2020 and
 644 a permanent 10% reduction onward:

$$\alpha(t) = \begin{cases} 1 & t < 2020 \\ 0.5 & 2020 \leq t < 2020.5 \\ 0.9 & 2020.5 \leq t \end{cases} \quad (12)$$

645 In both scenarios, we simulated the SIRS model from the ~~following same~~ initial
 646 conditions ($S(0) = 1/\mathcal{R}_0$, $I(0) = 1 \times 10^{-6}$, and $R(0) = 1 - S(0) - I(0)$) from 1900
 647 until 2030. ~~Throughout the paper, all deterministic models were solved using the~~
 648 ~~lsoda solver from the deSolve package [46] in R [47].~~

649 To measure the empirical resilience of the SIRS model (Figure 2C and 2F), we
 650 computed the normalized distance between post-intervention susceptible and logged
 651 infected proportions and their corresponding unperturbed values at the same time:

$$\sqrt{\left(\frac{S(t) - S_{\text{unperturbed}}(t)}{\sigma_S}\right)^2 + \left(\frac{\log I(t) - \log I_{\text{unperturbed}}(t)}{\sigma_{\log I}}\right)^2}, \quad (13)$$

652 where σ_S and $\sigma_{\log I}$ represent the standard deviation in the unperturbed susceptible
 653 and logged infected proportions. The unperturbed values were obtained by simulating
 654 the same SIRS model without pandemic perturbations ($\alpha = 1$). We normalized
 655 the differences in susceptible and logged infected proportions to allow both quantities
 656 to equally contribute to the changes in distance from the attractor. We used logged
 657 prevalence, instead of absolute prevalence, in order to capture epidemic dynamics
 658 in deep troughs during the intervention period. In Supplementary Materials, we
 659 also compared how the degree of seasonal transmission affects empirical resilience
 660 by varying θ from 0 to 0.4; when we assumed no seasonality ($\theta = 0$), we did not
 661 normalize the distance because the standard deviation of pre-intervention dynamics
 662 are zero.

663 We used the SIRS model to understand how underlying epidemiological parameters
 664 affect pathogen resilience and ~~link this determine the~~ relationship to underlying
 665 susceptible host dynamics. For the simple SIRS model without seasonal transmission
 666 ($\theta = 0$), the intrinsic resilience ~~corresponds to equals~~

$$-\frac{\text{Re}(\lambda)}{2} = \frac{\delta + \beta I^* + \mu}{2}. \quad (14)$$

667 Here, I^* represents the prevalence at endemic equilibrium:

$$I^* = \frac{(\delta + \mu)(\beta - (\gamma + \mu))}{\beta(\delta + \gamma + \mu)}. \quad (15)$$

668 The susceptible replenishment rate is given by

$$S_{\text{replenish}} = \frac{\mu + \delta R}{S^*}, \quad (16)$$

669 where $S^* = 1/\mathcal{R}_0$ represents the equilibrium proportion of susceptible individuals.
 670 We varied the basic reproduction number \mathcal{R}_0 between 1.1 to 6 and the average
 671 duration of immunity $1/\delta$ between 2 to 4 years, and computed these two quantities. In
 672 doing so, we fixed all other parameters: $\mu = 1/80/\text{years}$ and $\gamma = 365/7/\text{years}$. ~~When~~

673 infection provides a life-long immunity ($\delta = 0$), the intrinsic resilience is inversely
674 proportional to the susceptible replenishment rate:

$$\frac{\text{Re}(\lambda)}{2} = \frac{\mu}{2S^*} = \frac{S_{\text{replenish}}}{2}. \quad (17)$$

675 Finally, we used a seasonally unforced stochastic SIRS model without demog-
676 raphy to understand how pathogen resilience affects sensitivity of the system to
677 demographic stochasticity (see Supplementary Text for the details of the stochastic
678 SIRS model). By varying the basic reproduction number \mathcal{R}_0 between 2 to 20 and
679 the average duration of immunity $1/\delta$ between 1 to 40 years, we ran the ~~the~~ SIRS
680 model for 100 years and computed the epidemic amplitude, which we defined as
681 $(\max I - \min I)/(2\bar{I})$. Each simulation began from the equilibrium, and we truncated
682 ~~the~~ initial 25 years before computing the epidemic amplitude. In doing so,
683 we assumed $\gamma = 365/7/\text{years}$ and fixed the population size to 1 billion to prevent
684 any fadeouts. We also considered ~~using~~ a seasonally forced stochastic SIRS model
685 without demography, assuming an amplitude of seasonal forcing of 0.04; in this case,
686 we computed the relative epidemic amplitude by comparing the deterministic and
687 stochastic trajectories (Supplementary Materials).

688 Acknowledgement

689 We thank Anthony R. Ives and Stefano Allesina for helpful discussion. We thank
690 Centers for Disease Control and Prevention, National Respiratory and Enteric Virus
691 Surveillance System for providing respiratory case data in the US.

692 Data availability

693 All data and code are stored in a publicly available GitHub repository (<https://github.com/cobeylab/return-time>).

695 Funding

696 S.W.P. is a Peter and Carmen Lucia Buck Foundation Awardee of the Life Sciences
697 Research Foundation. B.F.N. acknowledges financial support from the Carlsberg
698 Foundation (grant no. CF23-0173). B.T.G. is supported by Princeton Catalysis
699 Initiative and Princeton Precision Health. S.C. is supported by Federal funds from
700 the National Institute of Allergy and Infectious Diseases, National Institutes of
701 Health, Department of Health and Human Services under CEIRR contract 75N93021C00015.
702 The content is solely the responsibility of the authors and does not necessarily
703 represent the official views of the NIAID or the National Institutes of Health. This
704 project has been funded in whole or in part with Federal funds from the National

705 Cancer Institute, National Institutes of Health, under Prime Contract No. 75N91019D00024,
706 Task Order No. 75N91023F00016 (B.F.N., E.H., and B.T.G). The content of this
707 publication does not necessarily reflect the views or policies of the Department of
708 Health and Human Services, nor does mention of trade names, commercial products
709 or organizations imply endorsement by the U.S. Government.

710 **Supplementary Text**

711 **Resilience of a stage-structured system.**

712 In Figure 2G–I, we used a more realistic, stage-structured model to illustrate how
 713 transient phenomena can cause the system to slow down. Specifically, we used the
 714 stage-structured RSV model proposed by [26], which assumes that subsequent rein-
 715 fections cause an individual to become less susceptible and transmissible than previ-
 716 ous infections. In contrast to a standard SIRS model, this model does not include a
 717 recovered compartment, which allow for temporary protection against new infections,
 718 and assumes that recoverd individuals are immediately susceptible to new infections.

719 The model dynamics can be described as follows:

$$\frac{dM}{dt} = \mu - (\omega + \mu)M \quad (S1)$$

$$\frac{dS_0}{dt} = \omega M - (\lambda(t) + \mu)S_0 \quad (S2)$$

$$\frac{dI_1}{dt} = \lambda(t)S_0 - (\gamma_1 + \mu)I_1 \quad (S3)$$

$$\frac{dS_1}{dt} = \gamma_1 I_1 - (\sigma_1 \lambda(t) + \mu)S_1 \quad (S4)$$

$$\frac{dI_2}{dt} = \sigma_1 \lambda(t)S_1 - (\gamma_2 + \mu)I_2 \quad (S5)$$

$$\frac{dS_2}{dt} = \gamma_2 I_2 - (\sigma_2 \lambda(t) + \mu)S_2 \quad (S6)$$

$$\frac{dI_3}{dt} = \sigma_2 \lambda(t)S_2 - (\gamma_3 + \mu)I_3 \quad (S7)$$

$$\frac{dS_3}{dt} = \gamma_3 I_3 - (\sigma_3 \lambda(t) + \mu)S_3 + \gamma_4 I_4 \quad (S8)$$

$$\frac{dI_4}{dt} = \sigma_3 \lambda(t)S_3 - (\gamma_4 + \mu)I_4 \quad (S9)$$

720 where M represents the proportion of individuals who are maternally immune; S_i
 721 represents the proportion of individuals who are susceptible after i prior infections; I_i
 722 represents the proportion of individuals who are currently (re)-infected with their i -th
 723 infection; μ represents the birth and death rates; $1/\omega$ represents the mean duration
 724 of maternal immunity; $1/\gamma_i$ represents the mean duration of infection; $\lambda(t)$ represents
 725 the force of infection; and σ_i represents the reduction in susceptibility for the i -th
 726 reinfection. The force of infection is modeled using a sinusoidal function:

$$\beta(t) = b_1(1 + \theta \cos(2\pi(t - \phi)))\alpha(t) \quad (S10)$$

$$\lambda(t) = \beta(I_1 + \rho_1 I_2 + \rho_2(I_3 + I_4)), \quad (S11)$$

727 where b_1 represents the baseline transmission rate; θ represents the seasonal ampli-
 728 tude; ϕ represents the seasonal offset term; $\alpha(t)$ represents the intervention effect;

and ρ_i represents the impact of immunity on transmission reduction. We used the following parameters to simulate the impact of interventions on epidemic dynamics [26]: $b_1 = 9 \times (365/10 + 1/80)/\text{years}$, $\theta = 0.2$, $\phi = -0.1$, $\omega = 365/112/\text{years}$, $\gamma_1 = 365/10/\text{years}$, $\gamma_2 = 365/7/\text{years}$, $\gamma_3 = 365/5/\text{years}$, $\sigma_1 = 0.76$, $\sigma_2 = 0.6$, $\sigma_3 = 0.4$, $\rho_1 = 0.75$, $\rho_2 = 0.51$, and $\mu = 1/80/\text{years}$. We assumed a 50% transmission reduction for 6 months from 2020:

$$\alpha(t) = \begin{cases} 0.5 & 2020 \leq t < 2020.5 \\ 1 & \text{otherwise} \end{cases} \quad (\text{S12})$$

The model was simulated from 1900 to 2030 using the following initial conditions: $M = 0$, $S_0 = 1/\mathcal{R}_0 - I_1$, $I_1 = 1 \times 10^{-6}$, $S_1 = 1 - 1/\mathcal{R}_0$, $I_2 = 0$, $S_2 = 0$, $I_3 = 0$, $S_3 = 0$, and $I_4 = 0$. For the phase plane analysis (Figure 2H) and distance analysis (Figure 2I), we relied on the average susceptibility,

$$\bar{S} = S_0 + \sigma_1 S_1 + \sigma_2 S_2 + \sigma_3 S_3, \quad (\text{S13})$$

and total prevalence,

$$I_{\text{total}} = I_1 + I_2 + I_3 + I_4. \quad (\text{S14})$$

These quantities were used to compute the normalized distance from the attractor, as described in the main text.

Resilience of a multistrain system.

We used a simple two-strain model to show that a multistrain host-pathogen system that is coupled through cross immunity can be described by a single resilience value. The model dynamics can be described as follows [34]:

$$\frac{dS}{dt} = \mu - \mu S - (\lambda_1 + \lambda_2)S + \underline{\rho} \underline{\delta}_1 R_1 + \underline{\rho} \underline{\delta}_2 R_2 \quad (\text{S15})$$

$$\frac{dI_1}{dt} = \lambda_1 S - (\gamma_1 + \mu)I_1 \quad (\text{S16})$$

$$\frac{dI_2}{dt} = \lambda_2 S - (\gamma_2 + \mu)I_2 \quad (\text{S17})$$

$$\frac{dR_1}{dt} = \gamma_1 I_1 - \lambda_2 \epsilon_{21} R_1 - \underline{\rho} \underline{\delta}_1 R_1 + \underline{\rho} \underline{\delta}_2 R - \mu R_1 \quad (\text{S18})$$

$$\frac{dR_2}{dt} = \gamma_2 I_2 - \lambda_1 \epsilon_{12} R_2 - \underline{\rho} \underline{\delta}_2 R_2 + \underline{\rho} \underline{\delta}_1 R - \mu R_2 \quad (\text{S19})$$

$$\frac{dJ_1}{dt} = \lambda_1 \epsilon_{12} R_2 - (\gamma_1 + \mu) J_1 \quad (\text{S20})$$

$$\frac{dJ_2}{dt} = \lambda_2 \epsilon_{21} R_1 - (\gamma_2 + \mu) J_2 \quad (\text{S21})$$

$$\frac{dR}{dt} = \gamma_1 J_1 + \gamma_2 J_2 - \underline{\rho} \underline{\delta}_1 R - \underline{\rho} \underline{\delta}_2 R - \mu R \quad (\text{S22})$$

where S represents the proportion of individuals who are fully susceptible to infections by both strains; I_1 represents the proportion of individuals who are infected with strain 1 without prior immunity; I_2 represents the proportion of individuals who are infected with strain 2 without prior immunity; R_1 represents the proportion of individuals who are fully immune against strain 1 and partially susceptible to reinfection by strain 2; R_2 represents the proportion of individuals who are fully immune against strain 2 and partially susceptible to reinfection by strain 1; J_1 represents the proportion of individuals who are infected with strain 1 with prior immunity against strain 2; J_2 represents the proportion of individuals who are infected with strain 2 with prior immunity against strain 1; R represents the proportion of individuals who are immune to infections from both strains; μ represents the birth/death rate; λ_1 and λ_2 represent the force of infection from strains 1 and 2, respectively; ρ_1 and ρ_2 represent the waning immunity rate; γ_1 and γ_2 represent the recovery rate; ϵ_{21} and ϵ_{12} represent the susceptibility to reinfection with strains 2 and 1, respectively, given prior immunity from infection with strains 1 and 2, respectively. The force of infection is modeled as follows:

$$\beta_1 = b_1(1 + \theta_1 \sin(2\pi(t - \phi_1)))\alpha(t) \quad (\text{S23})$$

$$\beta_2 = b_2(1 + \theta_2 \sin(2\pi(t - \phi_2)))\alpha(t) \quad (\text{S24})$$

$$\lambda_1 = \beta_1(I_1 + J_1) \quad (\text{S25})$$

$$\lambda_2 = \beta_2(I_2 + J_2) \quad (\text{S26})$$

In Supplementary Figures S2–S4, we assumed the following parameters: $b_1 = 2 \times 52/\text{years}$, $b_2 = 4 \times 52/\text{years}$, $\phi_1 = \phi_2 = 0$, $\epsilon_{12} = 0.9$, $\epsilon_{21} = 0.5$, $\gamma_1 = \gamma_2 = 52/\text{years}$, $\rho_1 = \rho_2 = 1/\text{years}$, $\delta_1 = \delta_2 = 1/\text{years}$, and $\mu = 1/70/\text{years}$. For all simulations, we assumed a 50% transmission reduction for 6 months from 2020:

$$\alpha(t) = \begin{cases} 0.5 & 2020 \leq t < 2020.5 \\ 1 & \text{otherwise} \end{cases} \quad (\text{S27})$$

The seasonal amplitude θ is varied from 0 to 0.4. All simulations were ran from 1900 to 2030 with following initial conditions: $S(0) = 1 - 2 \times 10^{-6}$, $I_1(0) = 1 \times 10^{-6}$, $I_2(0) = 1 \times 10^{-6}$, $R_1(0) = 0$, $R_2(0) = 0$, $J_1(0) = 0$, $J_2(0) = 0$, and $R(0) = 0$.

We considered three scenarios for measuring pathogen resilience: (1) we only have information about strain 1, (2) we only have information about strain 2, and (3) we are unable to distinguish between strains. In the first two scenarios (see panels A–C for strain 1 and panels D–F for strain 2), we considered the dynamics of average susceptibility for each strain and total prevalence:

$$\bar{S}_1 = S + \epsilon_{12}R_2 \quad (\text{S28})$$

$$\hat{I}_1 = I_1 + J_1 \quad (\text{S29})$$

$$\bar{S}_2 = S + \epsilon_{21}R_1 \quad (\text{S30})$$

$$\hat{I}_2 = I_2 + J_2 \quad (\text{S31})$$

⁷⁷⁴ In the third scenario (panels G–I), we considered the dynamics of total susceptible
⁷⁷⁵ and infected populations:

$$\hat{S} = S + R_2 + R_1 \quad (\text{S32})$$

$$\hat{I} = I_1 + J_1 + I_2 + J_2 \quad (\text{S33})$$

⁷⁷⁶ These quantities were used to compute the normalized distance from the attractor,
⁷⁷⁷ as described in the main text.

⁷⁷⁸ Estimating intrinsic resilience using a mechanistic model

⁷⁷⁹ We tested whether we can reliably estimate the intrinsic resilience of a system by fit-
⁷⁸⁰ ting a mechanistic model. Specifically, we simulated case time series from stochastic
⁷⁸¹ SIRS and two-strain models and fitted a simple, deterministic SIRS model using a
⁷⁸² Bayesian framework [4, 23, 48].

⁷⁸³ We simulated the models in discrete time with a daily time step ($\Delta t = 1$),
⁷⁸⁴ incorporating demographic stochasticity:

$$\beta(t) = \mathcal{R}_0 \left(1 + \theta \cos \left(\frac{2\pi t}{364} \right) \right) \alpha(t)(1 - \exp(-\gamma)) \quad (\text{S34})$$

$$\text{FOI}(t) = \beta(t)I(t - \Delta t)/N \quad (\text{S35})$$

$$B(t) \sim \text{Poisson}(\mu N) \quad (\text{S36})$$

$$\Delta S(t) \sim \text{Binom}(S(t - \Delta t), 1 - \exp(-(\text{FOI}(t) + \mu)\Delta t)) \quad (\text{S37})$$

$$N_{SI}(t) \sim \text{Binom}\left(\Delta S(t), \frac{\text{FOI}(t)}{\text{FOI}(t) + \mu}\right) \quad (\text{S38})$$

$$\Delta I(t) \sim \text{Binom}(I(t - \Delta t), 1 - \exp(-(\gamma + \mu)\Delta t)) \quad (\text{S39})$$

$$N_{IR}(t) \sim \text{Binom}\left(\Delta I(t), \frac{\gamma}{\gamma + \mu}\right) \quad (\text{S40})$$

$$\Delta R(t) \sim \text{Binom}(R(t - \Delta t), 1 - \exp(-(\delta + \mu)\Delta t)) \quad (\text{S41})$$

$$N_{RS}(t) \sim \text{Binom}\left(\Delta R(t), \frac{\delta}{\delta + \mu}\right) \quad (\text{S42})$$

$$S(t) = S(t - \Delta t) + N_{RS}(t) + B(t) - \Delta S(t) \quad (\text{S43})$$

$$I(t) = I(t - \Delta t) + N_{SI}(t) - \Delta I(t) \quad (\text{S44})$$

$$R(t) = R(t - \Delta t) + N_{IR}(t) - \Delta R(t) \quad (\text{S45})$$

⁷⁸⁵ where FOI ~~represent-represents~~ the force of infection; N_{ij} ~~represent-represents~~ the
⁷⁸⁶ number of individuals moving from compartment i to j on a given day; and $B(t)$
⁷⁸⁷ represents the number of new births. All other parameters definitions can be found
⁷⁸⁸ in the description of the deterministic version of the model. We simulated the model
⁷⁸⁹ on a daily scale—assuming 364 days in a year so that it can be evenly grouped
⁷⁹⁰ into 52 weeks—with the following parameters: $\mathcal{R}_0 = 3$, $\theta = 0.1$, $\gamma = 1/7/\text{days}$, $\delta =$

⁷⁹¹ $1/(364 \times 2)$ /days, $\mu = 1/(364 \times 50)$ /days, and $N = 1 \times 10^8$. The model was simulated
⁷⁹² from 1900 to 2030 assuming $S(0) = N/3$, $I(0) = 100$, and $R(0) = N - S(0) - I(0)$.
⁷⁹³ The observed incidence from the model was then simulated as follows:

$$C(t) = \text{Beta-Binom}(N_{SI}(t), \rho, k), \quad (\text{S46})$$

⁷⁹⁴ where ρ represents the reporting probability and k represents the overdispersion
⁷⁹⁵ parameter of beta-binomial distribution. Here, we used the beta-binomial distribu-
⁷⁹⁶ tion to account for overdispersion in reporting. We assumed $\rho = 0.002$ (i.e., 0.2%
⁷⁹⁷ probability) and $k = 1000$.

⁷⁹⁸ We used an analogous approach for the two-strain model:

$$\beta_1(t) = b_1 \left(1 + \theta_1 \cos \left(\frac{2\pi(t - \phi_1)}{364} \right) \right) \alpha(t) \quad (\text{S47})$$

$$\beta_2(t) = b_2 \left(1 + \theta_2 \cos \left(\frac{2\pi(t - \phi_2)}{364} \right) \right) \alpha(t) \quad (\text{S48})$$

$$\text{FOI}_1(t) = \beta_1(t)(I_1(t - \Delta t) + J_1(t - \Delta t))/N \quad (\text{S49})$$

$$\text{FOI}_2(t) = \beta_2(t)(I_2(t - \Delta t) + J_2(t - \Delta t))/N \quad (\text{S50})$$

$$B(t) \sim \text{Poisson}(\mu N) \quad (\text{S51})$$

$$\Delta S(t) \sim \text{Binom}(S(t - \Delta t), 1 - \exp(-(\text{FOI}_1(t) + \text{FOI}_2(t) + \mu)\Delta t)) \quad (\text{S52})$$

$$N_{SI_1}(t) \sim \text{Binom}\left(\Delta S(t), \frac{\text{FOI}_1(t)}{\text{FOI}_1(t) + \text{FOI}_2(t) + \mu}\right) \quad (\text{S53})$$

$$N_{SI_2}(t) \sim \text{Binom}\left(\Delta S(t), \frac{\text{FOI}_2(t)}{\text{FOI}_1(t) + \text{FOI}_2(t) + \mu}\right) \quad (\text{S54})$$

$$\Delta I_1(t) \sim \text{Binom}(I_1(t - \Delta t), 1 - \exp(-(\gamma_1 + \mu)\Delta t)) \quad (\text{S55})$$

$$N_{I_1 R_1}(t) \sim \text{Binom}\left(\Delta I_1(t), \frac{\gamma_1}{\gamma_1 + \mu}\right) \quad (\text{S56})$$

$$\Delta I_2(t) \sim \text{Binom}(I_2(t - \Delta t), 1 - \exp(-(\gamma_2 + \mu)\Delta t)) \quad (\text{S57})$$

$$N_{I_2 R_2}(t) \sim \text{Binom}\left(\Delta I_2(t), \frac{\gamma_2}{\gamma_2 + \mu}\right) \quad (\text{S58})$$

$$\Delta R_1(t) \sim \text{Binom}(R_1(t - \Delta t), 1 - \exp(-(\epsilon_{21}\text{FOI}_2(t) + \rho_1 + \mu)\Delta t)) \quad (\text{S59})$$

$$N_{R_1 S}(t) \sim \text{Binom}\left(\Delta R_1(t), \frac{\rho_1}{\epsilon_{21}\text{FOI}_2(t) + \rho_1 + \mu}\right) \quad (\text{S60})$$

$$N_{R_1 J_2}(t) \sim \text{Binom}\left(\Delta R_1(t), \frac{\epsilon_{21}\text{FOI}_2(t)}{\epsilon_{21}\text{FOI}_2(t) + \rho_1 + \mu}\right) \quad (\text{S61})$$

$$\Delta R_2(t) \sim \text{Binom}(R_2(t - \Delta t), 1 - \exp(-(\epsilon_{12}\text{FOI}_1(t) + \rho_2 + \mu)\Delta t)) \quad (\text{S62})$$

$$N_{R_2 S}(t) \sim \text{Binom}\left(\Delta R_2(t), \frac{\rho_2}{\epsilon_{12}\text{FOI}_1(t) + \rho_2 + \mu}\right) \quad (\text{S63})$$

$$N_{R_2 J_1}(t) \sim \text{Binom}\left(\Delta R_2(t), \frac{\epsilon_{12}\text{FOI}_1(t)}{\epsilon_{12}\text{FOI}_1(t) + \rho_2 + \mu}\right) \quad (\text{S64})$$

$$\Delta J_1(t) \sim \text{Binom}(J_1(t - \Delta t), 1 - \exp(-(\gamma_1 + \mu)\Delta t)) \quad (\text{S65})$$

$$N_{J_1R}(t) \sim \text{Binom}\left(\Delta J_1(t), \frac{\gamma_1}{\gamma_1 + \mu}\right) \quad (\text{S66})$$

$$\Delta J_2(t) \sim \text{Binom}(J_2(t - \Delta t), 1 - \exp(-(\gamma_2 + \mu)\Delta t)) \quad (\text{S67})$$

$$N_{J_2R}(t) \sim \text{Binom}\left(\Delta J_2(t), \frac{\gamma_2}{\gamma_2 + \mu}\right) \quad (\text{S68})$$

$$\Delta R(t) \sim \text{Binom}(R(t - \Delta t), 1 - \exp(-(\rho_1 + \rho_2 + \mu)\Delta t)) \quad (\text{S69})$$

$$N_{RR_1}(t) \sim \text{Binom}\left(\Delta R(t), \frac{\rho_1}{\rho_1 + \rho_2 + \mu}\right) \quad (\text{S70})$$

$$N_{RR_2}(t) \sim \text{Binom}\left(\Delta R(t), \frac{\rho_2}{\rho_1 + \rho_2 + \mu}\right) \quad (\text{S71})$$

$$S(t) = S(t - \Delta t) - \Delta S(t) + B(t) + N_{R_1S}(t) + N_{R_2S}(t) \quad (\text{S72})$$

$$I_1(t) = I_1(t - \Delta t) - \Delta I_1(t) + N_{SI_1}(t) \quad (\text{S73})$$

$$I_2(t) = I_2(t - \Delta t) - \Delta I_2(t) + N_{SI_2}(t) \quad (\text{S74})$$

$$R_1(t) = R_1(t - \Delta t) - \Delta R_1(t) + N_{I_1R_1}(t) + N_{RR_1}(t) \quad (\text{S75})$$

$$R_2(t) = R_2(t - \Delta t) - \Delta R_2(t) + N_{I_2R_2}(t) + N_{RR_2}(t) \quad (\text{S76})$$

$$J_1(t) = J_1(t - \Delta t) - \Delta J_1(t) + N_{R_2J_1}(t) \quad (\text{S77})$$

$$J_2(t) = J_2(t - \Delta t) - \Delta J_2(t) + N_{R_1J_2}(t) \quad (\text{S78})$$

$$R(t) = R(t - \Delta t) - \Delta R(t) + N_{J_1R}(t) + N_{J_2R}(t) \quad (\text{S79})$$

799 We simulated the model on a daily scale with previously estimated parameters for the
 800 RSV-HMPV interaction [34]: $b_1 = 1.7/\text{weeks}$, $b_2 = 1.95/\text{weeks}$, $\theta_1 = 0.4$, $\theta_2 = 0.3$,
 801 $\phi_1 = 0.005 \times 7/364$, $\phi_2 = 4.99 \times 7/364$, $\epsilon_{12} = 0.92$, $\epsilon_{21} = 0.45$, $\gamma_1 = 1/10/\text{days}$,
 802 $\gamma_2 = 1/10/\text{days}$, $\rho_1 = 1/364/\text{days}$, $\rho_2 = 1/364/\text{days}$, $\mu = 1/(70 \times 364)/\text{days}$, and
 803 $N = 1 \times 10^8$. The model was simulated from 1900 to 2030 assuming $S(0) = N - 200$,
 804 $I_1(0) = 100$, $I_2(0) = 100$, $R_1(0) = 0$, $R_2(0) = 0$, $J_1(0) = 0$, $J_2(0) = 0$, and $R(0) = 0$.
 805 The observed incidence for each strain is then simulated as follows:

$$C_1(t) = \text{Beta-Binom}(N_{SI_1}(t) + N_{R_2J_1}, \rho, k), \quad (\text{S80})$$

$$C_2(t) = \text{Beta-Binom}(N_{SI_2}(t) + N_{R_1J_2}, \rho, k), \quad (\text{S81})$$

806 where ρ represents the reporting probability and k represents the overdispersion pa-
 807 rameter of beta-binomial distribution. We assumed $\rho = 0.002$ (i.e., 0.2% probability)
 808 and $k = 500$. We also considered the total incidence: $C_{\text{total}}(t) = C_1(t) + C_2(t)$.

809 For both models, we considered a more realistically shaped pandemic pertur-
 810 bation $\alpha(t)$ to challenge our ability to estimate the intervention effects. Thus, we
 811 assumed a 40% transmission reduction for 3 months from March 2020, followed by a
 812 10% transmission reduction for 6 months, 20% transmission reduction for 3 months,

813 and a final return to normal levels:

$$\alpha(t) = \begin{cases} 1 & t < 2020.25 \\ 0.6 & 2020.25 \leq t < 2020.5 \\ 0.9 & 2020.5 \leq t < 2021 \\ 0.8 & 2021 \leq t < 2021.25 \\ 1 & 2021.25 \leq t \end{cases}. \quad (\text{S82})$$

814 For all simulations, we truncated the time series from the beginning of 2014 to the
 815 end of 2023 and ~~aggregate-aggregated~~ them into weekly cases.

816 To infer intrinsic resilience from time series, we fitted a simple discrete time,
 817 deterministic SIRS model in a Bayesian framework [4]:

$$\Delta t = 1 \text{ week} \quad (\text{S83})$$

$$\text{FOI}(t) = \beta(t)(I(t - \Delta t) + \omega)/N \quad (\text{S84})$$

$$\Delta S(t) = [1 - \exp(-(\text{FOI}(t) + \mu)\Delta t)] S(t - \Delta t) \quad (\text{S85})$$

$$N_{SI}(t) = \frac{\text{FOI}(t)\Delta S(t)}{\text{FOI}(t) + \mu} \quad (\text{S86})$$

$$\Delta I(t) = [1 - \exp(-(\gamma + \mu)\Delta t)] I(t - \Delta t) \quad (\text{S87})$$

$$N_{IR}(t) = \frac{\gamma \Delta I(t)}{\gamma + \mu} \quad (\text{S88})$$

$$\Delta R(t) = [1 - \exp(-(\nu + \mu)\Delta t)] R(t - \Delta t) \quad (\text{S89})$$

$$N_{RS}(t) = \frac{\nu \Delta R(t)}{\nu + \mu} \quad (\text{S90})$$

$$S(t) = S(t - \Delta t) + \mu S - \Delta S(t) + N_{RS}(t) \quad (\text{S91})$$

$$I(t) = I(t - \Delta t) - \Delta I(t) + N_{SI}(t) \quad (\text{S92})$$

$$R(t) = R(t - \Delta t) - \Delta R(t) + N_{IR}(t) \quad (\text{S93})$$

818 where we include an extra term ω to account for ~~external infections~~importation.
 819 Although actual simulations did not include any ~~external infections~~, we importation,
 820 we had found that including this term generally helped with model convergence in
 821 previous analyses [4]. The transmission rate was divided into a seasonal term $\beta_{\text{seas}}(t)$
 822 (repeated every year) and intervention term $\alpha(t)$, which were estimated jointly:

$$\beta(t) = \beta_{\text{seas}}(t)\alpha(t), \quad (\text{S94})$$

823 where $\alpha < 1$ corresponds to reduction in transmission due to intervention effects. To
 824 constrain the smoothness of $\beta_{\text{seas}}(t)$, we imposed cyclic, random-walk priors:

$$\beta_{\text{seas}}(t) \sim \text{Normal}(\beta_{\text{seas}}(t - 1), \sigma) \quad t = 2 \dots 52 \quad (\text{S95})$$

$$\beta_{\text{seas}}(1) \sim \text{Normal}(\beta_{\text{seas}}(52), \sigma) \quad (\text{S96})$$

$$\underline{\sigma} \approx \text{Half-Normal}(0, 1) \quad (\text{S97})$$

825 We fixed $\alpha(t) = 1$ for all $t < 2020$ and estimate α assuming a normal prior:

$$\alpha \sim \text{Normal}(1, 0.25). \quad (\text{S98})$$

826 We assumed weakly informative priors on ω and ν :

$$\omega \sim \text{Normal}(0, 200) \text{Half-Normal}(0, 200) \quad (\text{S99})$$

$$\nu \sim \text{Normal}(104, 26) \quad (\text{S100})$$

827 We assumed that the true birth/death rates, population sizes, and recovery rates
828 are known. We note, however, that assuming $\gamma = 1/\text{week}$ actually corresponds to
829 a mean simulated infectious period of 1.6 weeks due to a time discretization, which
830 is much longer than the true value; this approximation allows us to test whether we
831 can still robustly estimate the intrinsic resilience given parameter mis-specification.
832 Initial conditions were estimated with following priors:

$$S(0) = Ns(0) \quad (\text{S101})$$

$$I(0) = Ni(0) \quad (\text{S102})$$

$$s(0) \sim \text{Uniform}(0, 1) \quad (\text{S103})$$

$$i(0) \sim \text{Half-Normal}(0, 0.001) \quad (\text{S104})$$

833 Finally, the observation model was specified as follows:

$$\text{Cases}(t) \sim \text{Negative-Binomial}(\rho N_{SI}(t), \phi) \quad (\text{S105})$$

$$\rho \sim \text{Half-Normal}(0, 0.02) \quad (\text{S106})$$

$$\phi \sim \text{Half-Normal}(0, 10) \quad (\text{S107})$$

834 where ρ represents the reporting probability and ϕ represents the negative binomial
835 overdispersion parameter.

836 The model was fitted to four separate time series: (1) incidence time series from
837 the SIRS model, (2) incidence time series for strain 1 from the two-strain model,
838 (3) incidence time series for strain 2 from the two-strain model, and (4) combined
839 incidence time series for strains 1 and 2 from the two-strain model. The model was
840 fitted using rstan [49, 50] with 4 chains, each consisting of 2000 iterations. The
841 resulting posterior distribution was used to calculate the intrinsic resilience of the
842 seasonally unforced ~~system~~-SIRS model with the same parameters; eigenvalues of the
843 discrete-time SIR model were computed by numerically finding the equilibrium and
844 calculating the Jacobian matrix.

845 **Validations for window-selection criteria**

846 We used stochastic SIRS simulations to identify optimal parameters for the window-
847 selection criteria that we used for the linear regression for estimating empirical re-
848 silience. For each simulation, we began by generating a random perturbation $\alpha(t)$

849 from a random set of parameters. First, we drew the duration of perturbation τ_{npi}
 850 from a uniform distribution between 1 and 2 years. Then, we drew independent
 851 normal variables z_i of length $\lfloor 364\tau_{\text{npi}} \rfloor$ with a standard deviation of 0.02 and took a
 852 reverse cumulative sum to obtain a realistic shape for the perturbation:

$$x_n = 1 + \sum_{i=n}^{\lfloor 364\tau_{\text{npi}} \rfloor} z_i, \quad n = 1, \dots, \lfloor 364\tau_{\text{npi}} \rfloor. \quad (\text{S108})$$

853 In contrast to simple perturbations that assume a constant reduction in transmission,
 854 this approach allows us to model transmission reduction that varies over time smoothly.
 855 We repeated this random generation process until less than 10% of x_n exceeds 1—this
 856 was done to ~~prevent the perturbation~~ ensure the perturbation term $\alpha(t)$ stays below
 857 1 (and therefore reduce transmission) for the most part. Then, we set any values
 858 that are above 1 or below 0 ~~as to~~ 1 and 0, respectively. Then, we randomly drew the
 859 minimum transmission during perturbation α_{\min} from a uniform distribution between
 860 0.5 and 0.7 and scale x_n to have a minimum of α_{\min} :

$$x_{\text{scale},n} = \alpha_{\min} + (1 - \alpha_{\min}) \times \frac{x_n - \min x_n}{1 - \min x_n}. \quad (\text{S109})$$

861 This allowed us to simulate a realistically shaped perturbation:

$$\alpha(t) = \begin{cases} 1 & t < 2020 \\ x_{\text{scale},364(t-2020)} & 2020 \leq t < 2020 + \tau_{\text{npi}} \\ 1 & \tau_{\text{npi}} \leq t \end{cases}. \quad (\text{S110})$$

862 Given this perturbation function, we draw \mathcal{R}_0 from a uniform distribution between
 863 1.5 and 4 and the mean duration of immunity $1/\delta$ from a uniform distribution be-
 864 tween 1 and 4. Then, we simulate the stochastic SIRS model from $S(0) = 10^8/\mathcal{R}_0$
 865 and $I(0) = 100$ from 1990 to 2025 and truncate the time series to 2014–2025; if the
 866 epidemic becomes extinct before the end of simulation, we discard that simulation
 867 and start over from the perturbation generation step.

868 For each epidemic simulation, we computed the empirical resilience by varying
 869 the threshold R for the nearest neighbor approach from 4 to 14 with increments of
 870 2, the number of divisions K for the window selection between 8 and 25, and the
 871 truncation threshold a for the window selection between 1 to 3; this was done for all
 872 possible combinations of R , K , and a . We also compared this with the naive approach
 873 that uses the entire distance-from-attractor time series, starting from the maximum
 874 distance to the end of the time series. We repeated this procedure 500 times and
 875 quantified the correlation between empirical and intrinsic resilience estimates across
 876 two approaches.

Supplementary Figures

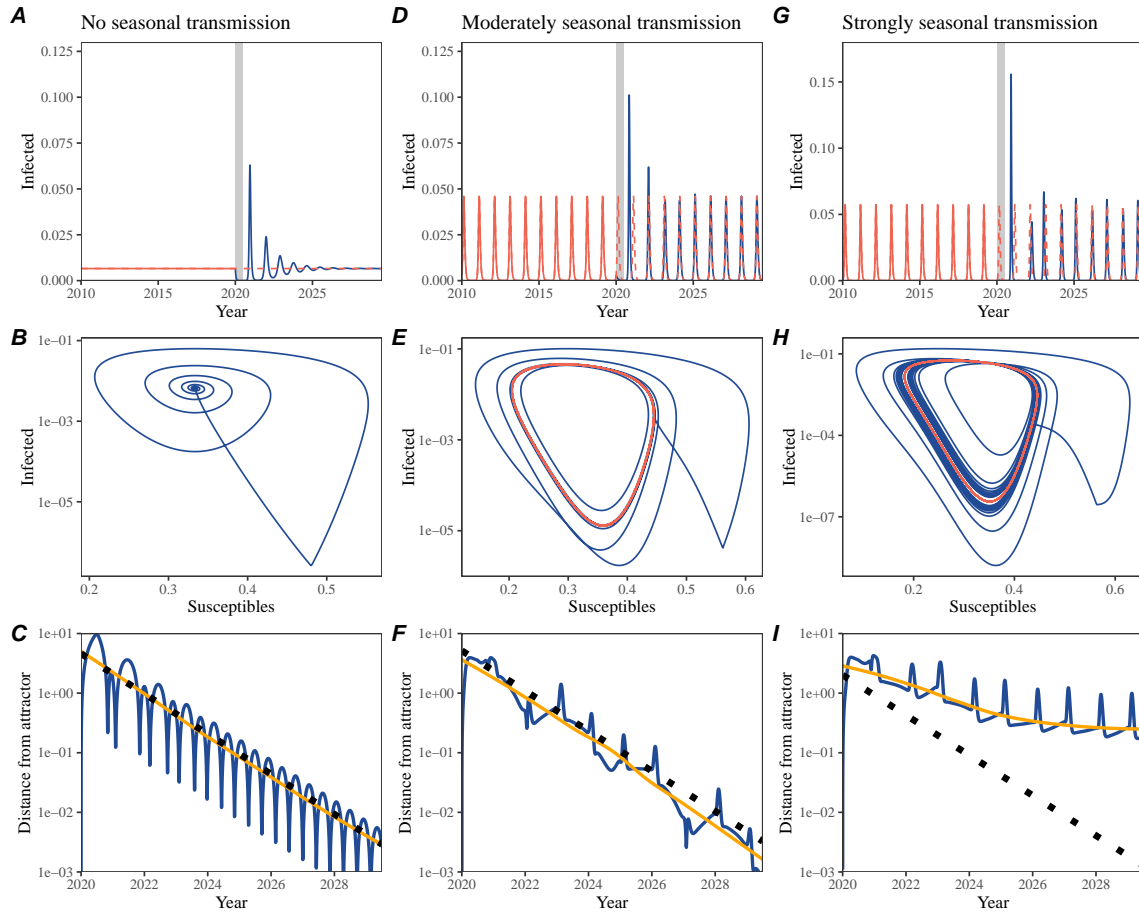


Figure S1: Impact of seasonal transmission on pathogen resilience. (A, D, G) Simulated epidemic trajectories using the SIRS model without seasonal forcing (A), with seasonal forcing of amplitude of 0.2 (D), and with seasonal forcing of amplitude of 0.4 (G). Red and blue solid lines represent epidemic dynamics before and after interventions are introduced, respectively. Red dashed lines represent counterfactual epidemic dynamics in the absence of interventions. Gray regions indicate the duration of interventions. (B, E, H) Phase plane representation of the time series in panels A, D, and G alongside the corresponding susceptible host dynamics. Red and blue solid lines represent epidemic trajectories on an SI phase plane before and after interventions are introduced, respectively. (C, F, I) Changes in logged distance from the attractor over time. Blue lines represent the logged distance from the attractor. Orange lines represent the locally estimated scatterplot smoothing (LOESS) fits to the logged distance from the attractor. Dotted lines show the intrinsic resilience of the seasonally unforced system.

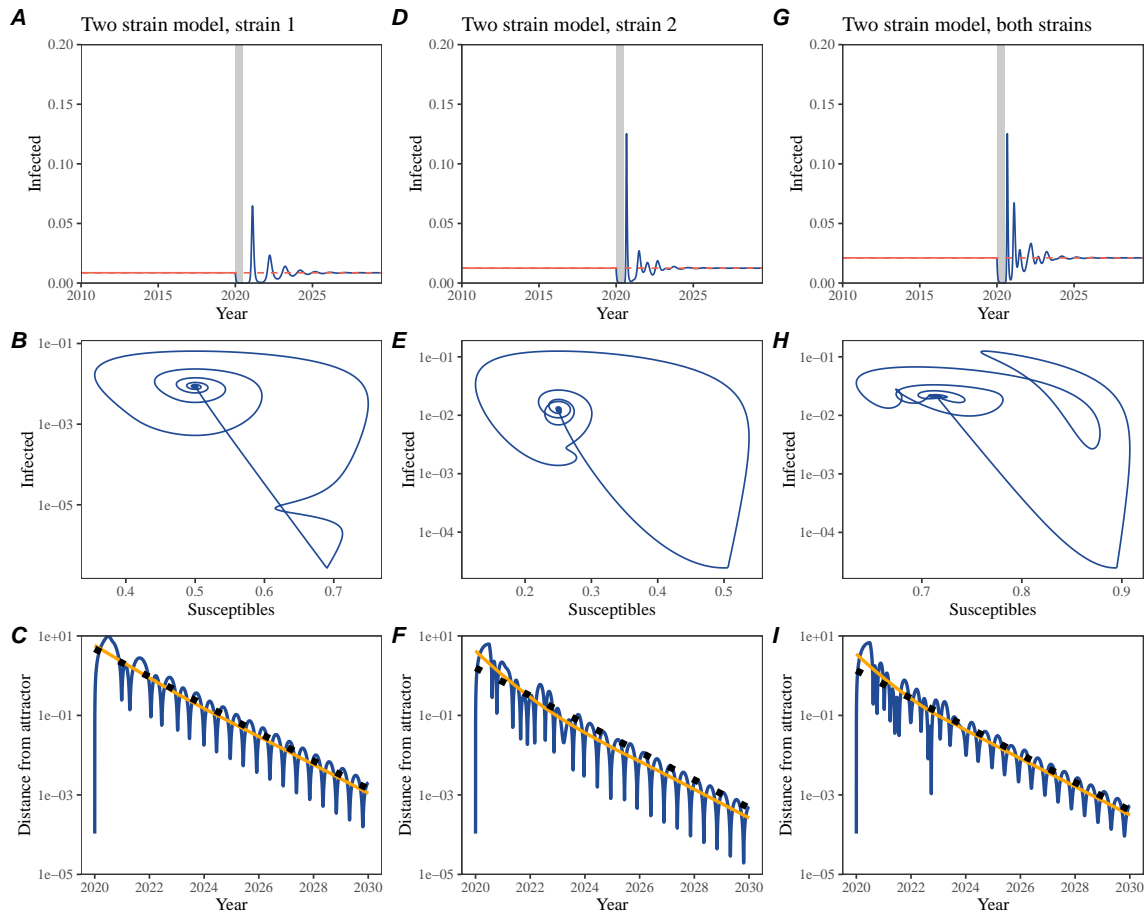


Figure S2: **A simple method to measure pathogen resilience following pandemic perturbations for a two-strain system without seasonal forcing.**
A simple method to measure pathogen resilience following pandemic perturbations for a two-strain competition system without seasonal forcing. (A, D, G) Simulated epidemic trajectories using a ~~multi-strain~~ two-strain system without seasonal forcing. In this model, two strains compete through cross immunity. Red and blue solid lines represent epidemic dynamics before and after interventions are introduced, respectively. Red dashed lines represent counterfactual epidemic dynamics in the absence of interventions. Gray regions indicate the duration of interventions. (B, E, H) Phase plane representation of the time series in panels A, D, and G alongside the corresponding susceptible host dynamics. Blue solid lines represent epidemic trajectories on an SI phase plane before and after interventions are introduced, respectively. (C, F, I) Changes in logged distance from the attractor over time. Blue lines represent the logged distance from the attractor. Orange lines represent the locally estimated scatterplot smoothing (LOESS) fits to the logged distance from the attractor. Dotted lines show the intrinsic resilience of the seasonally unforced system.

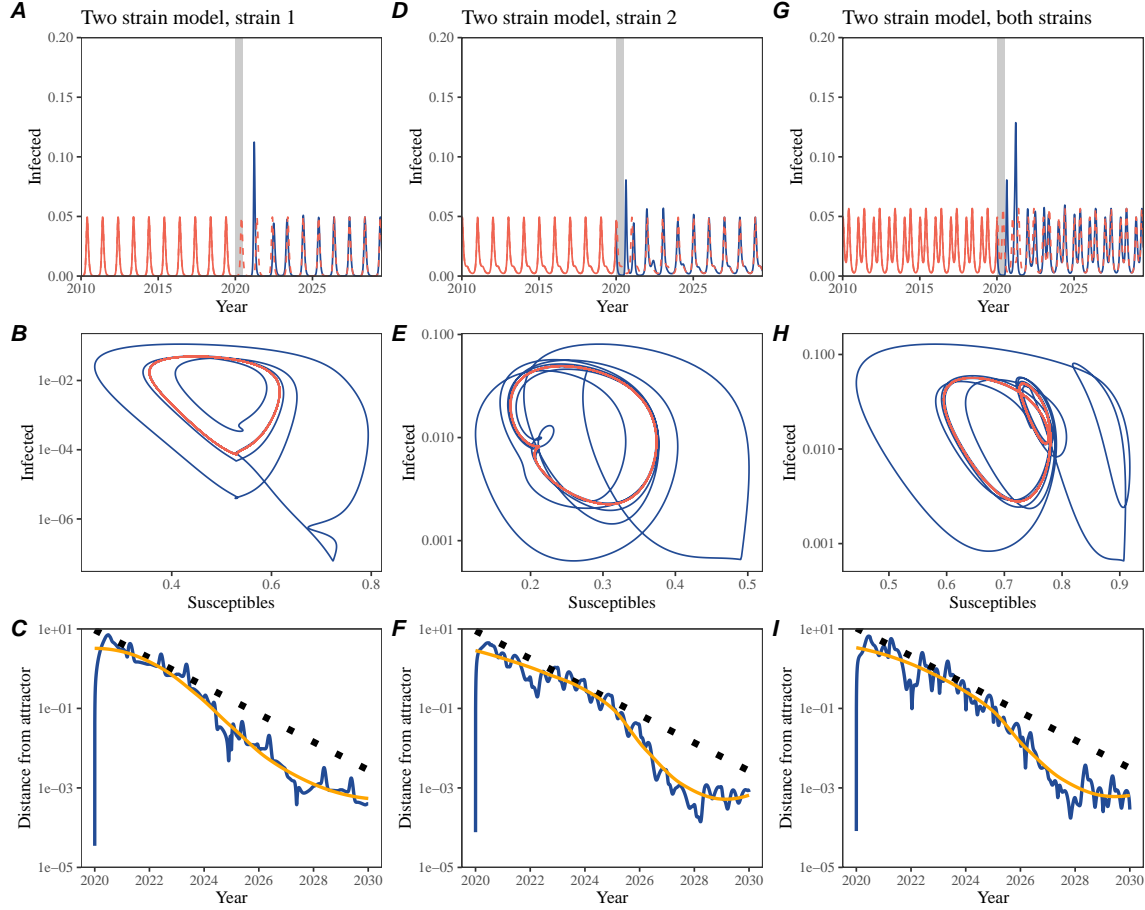


Figure S3: A simple method to measure pathogen resilience following pandemic perturbations for a two-strain system with seasonal forcing. A simple method to measure pathogen resilience following pandemic perturbations for a two-strain competition system with seasonal forcing.

(A, D, G) Simulated epidemic trajectories using a two-strain system with seasonal forcing (amplitude of 0.2). In this model, two strains compete through cross immunity. Red and blue solid lines represent epidemic dynamics before and after interventions are introduced, respectively. Red dashed lines represent counterfactual epidemic dynamics in the absence of interventions. Gray regions indicate the duration of interventions. (B, E, H) Phase plane representation of the time series in panels A, D, and G alongside the corresponding susceptible host dynamics. Red and blue solid lines represent epidemic trajectories on an SI phase plane before and after interventions are introduced, respectively. (C, F, I) Changes in logged distance from the attractor over time. Blue lines represent the logged distance from the attractor. Orange lines represent the locally estimated scatterplot smoothing (LOESS) fits to the logged distance from the attractor. Dotted lines show the intrinsic resilience of the seasonally unforced system.

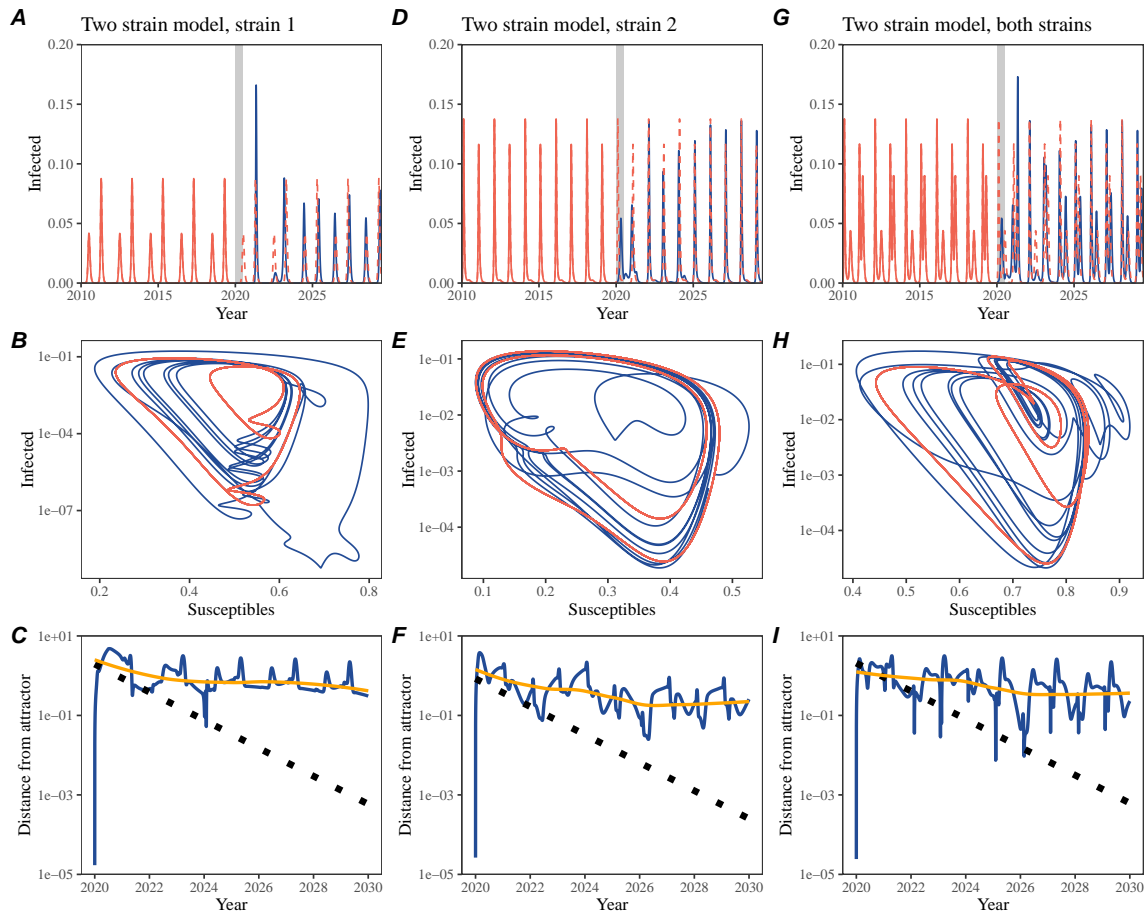


Figure S4: **A simple method to measure pathogen resilience following pandemic perturbations for a multi-strain system with strong seasonal forcing. A simple method to measure pathogen resilience following pandemic perturbations for a multi-strain competition system with strong seasonal forcing.** (A, D, G) Simulated epidemic trajectories using a multi-strain two-strain system with seasonal forcing (amplitude of 0.40.2). In this model, two strains compete through cross immunity. Red and blue solid lines represent epidemic dynamics before and after interventions are introduced, respectively. Red dashed lines represent counterfactual epidemic dynamics in the absence of interventions. Gray regions indicate the duration of interventions. (B, E, H) Phase plane representation of the time series in panels A, D, and G alongside the corresponding susceptible host dynamics. Red and blue solid lines represent epidemic trajectories on an SI phase plane before and after interventions are introduced, respectively. (C, F, I) Changes in logged distance from the attractor over time. Blue lines represent the logged distance from the attractor. Orange lines represent the locally estimated scatterplot smoothing (LOESS) fits to the logged distance from the attractor. Dotted lines show the intrinsic resilience of the seasonally unforced system.

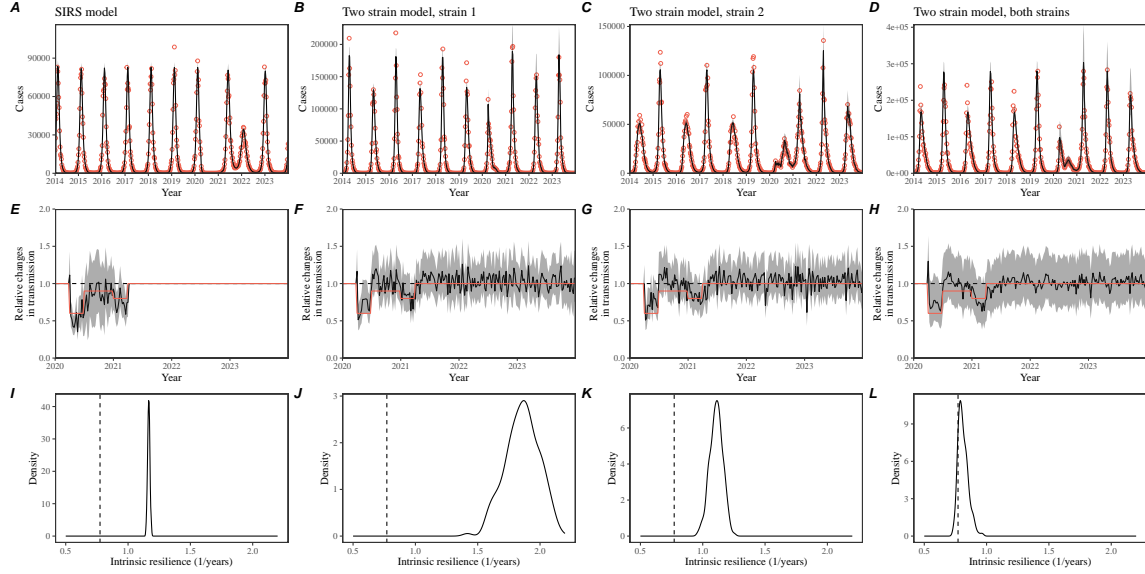


Figure S5: Mechanistic model fits to simulated data and inferred intrinsic resilience. We simulated discrete time, stochastic epidemic trajectories using [a](#) seasonally forced SIRS model (A,E,I) and [a](#) seasonally forced two-strain model (B–D, F–H, and J–L) and tested whether we can estimate the intrinsic resilience of the seasonally unforced versions of the model by fitting a mechanistic model (Supplementary Text). We fitted the same discrete time, [one strain](#), deterministic SIRS model ~~across all four scenarios in each scenario~~. (A–D) Simulated case time series from corresponding models shown in the title (red) and SIRS model fits (black). (E–H) Assumed changes in transmission due to pandemic perturbations (red) and estimated time-varying relative transmission rates for the perturbation impact from the SIRS model fits (black). Solid lines and shaded regions represent fitted posterior median and 95% credible intervals. (I–L) [True Comparisons between the true and estimated](#) intrinsic resilience of the seasonally unforced system ~~(vertical –)~~. Vertical lines ~~) and represent~~ the [true intrinsic resilience of the seasonally unforced system](#). Density plots represent the [posterior distribution of the inferred intrinsic resilience from](#) of the [seasonally unforced](#) SIRS model ([density plots](#))[using fitted parameters](#).

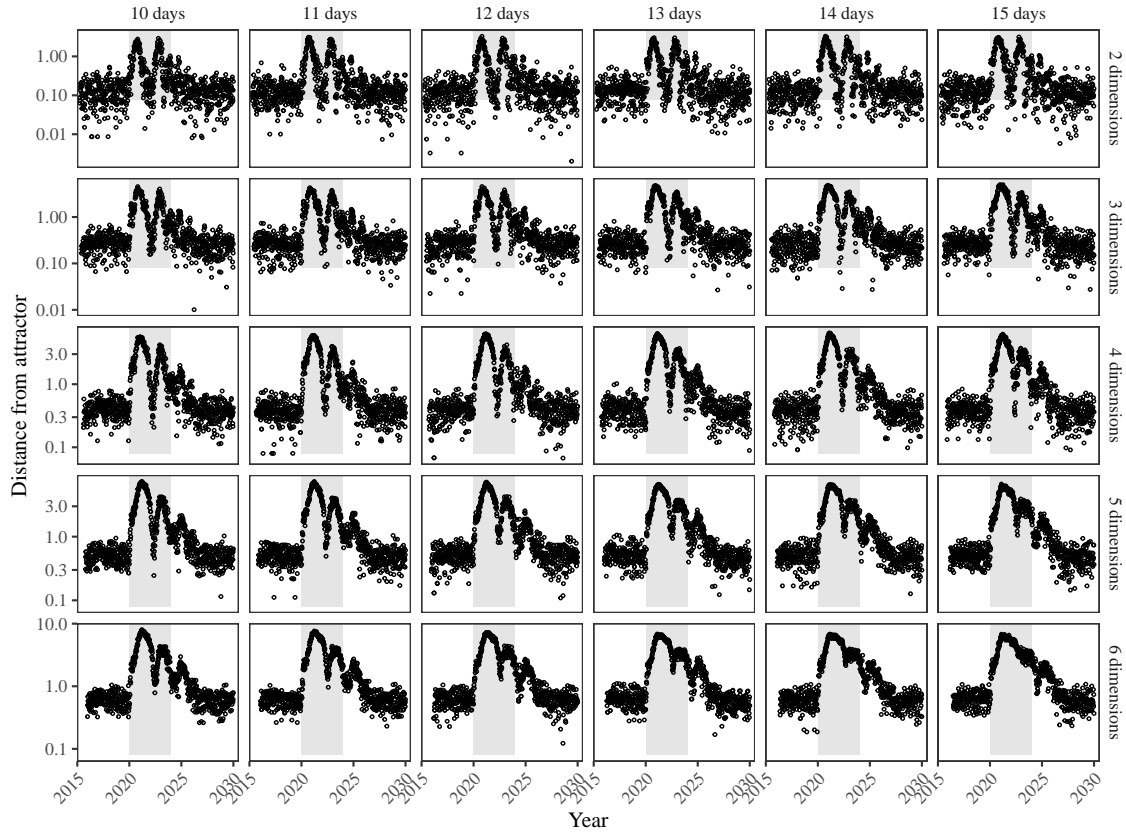


Figure S6: ~~Sensitivity of the distance from the attractor to choices about embedding lags and dimensions.~~ Sensitivity of the distance from the attractor to choice of embedding lags and dimensions. Sensitivity analysis for the distance-from-attractor time series shown in Figure 3E in the main text by varying the embedding lag between 10–15 days and embedding dimensions between 2–6 dimensions. The gray region represents the assumed period of pandemic perturbation.

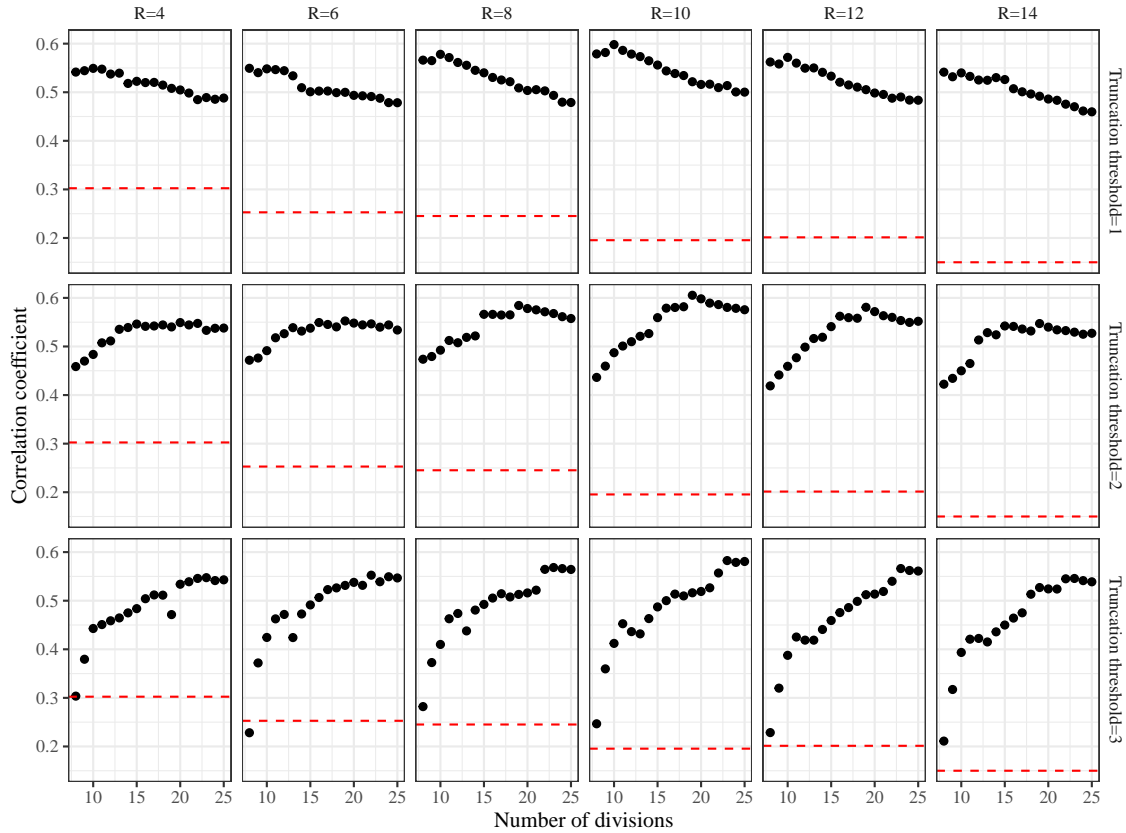


Figure S7: Impact of fitting window selection on the estimation of empirical resilience. We simulated 500 epidemics of a stochastic SIRS model with randomly drawn parameters and randomly generated pandemic perturbations (Supplementary Text). For each simulation, we varied the false nearest neighbor threshold R for reconstructing the empirical attractor as well as the parameters for regression window selection (i.e., the truncation threshold a and the ~~the~~-number of divisions K). Each point represents the resulting correlation coefficient between empirical and intrinsic resilience estimates for a given scenario. Dashed lines represent the correlation coefficient between empirical and intrinsic resilience estimates for the naive approach that fits a linear regression on a log scale, starting from the maximum distance until the end of the time series.

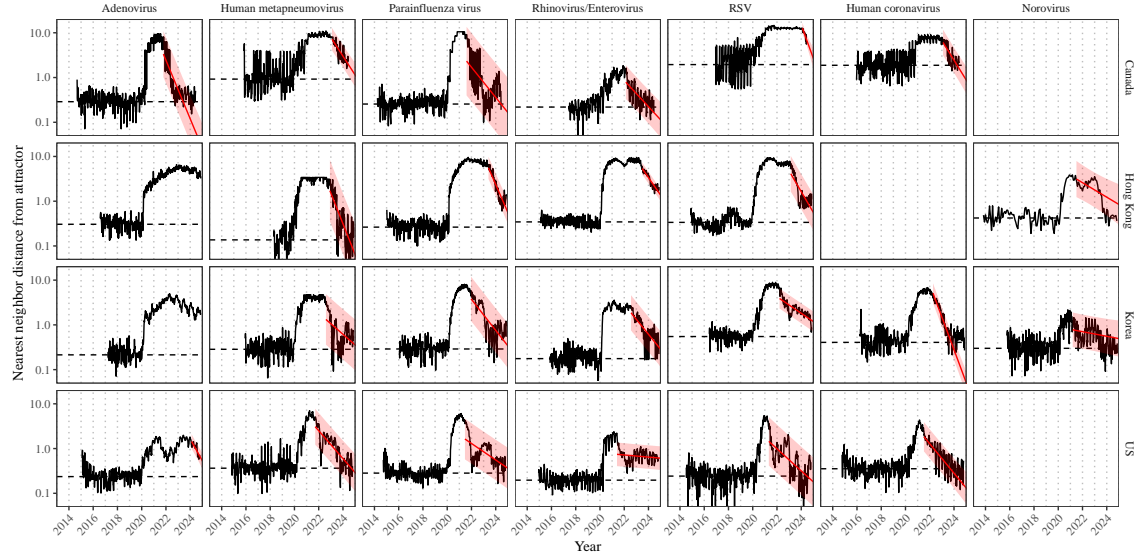


Figure S8: Estimated time series of distance from the attractor for each pathogen and corresponding linear regression fits using automated window selection criterion across Canada, Hong Kong, Korea, and the US. Black lines represent the estimated distance from the attractor. Red lines and shaded regions represent the linear regression fits and corresponding 95% confidence intervals. Dashed lines represent the average of the pre-pandemic nearest neighbor distances.

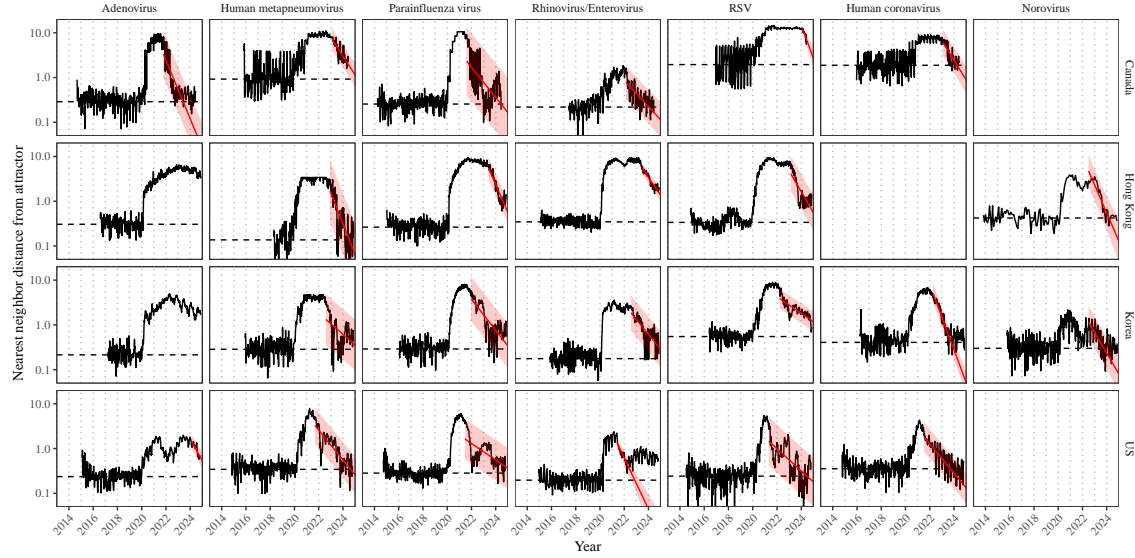


Figure S9: **Estimated time series of distance from the attractor for each pathogen and corresponding linear regression fits across Canada, Hong Kong, Korea, and the US, including ad-hoc regression window selection.** We used ad-hoc regression windows for norovirus in Hong Kong and Korea and Rhinovirus/Enterovirus in the US. Black lines represent the estimated distance from the attractor. Red lines and shaded regions represent the linear regression fits and corresponding 95% confidence intervals. Dashed lines represent the average of the pre-pandemic nearest neighbor distances.

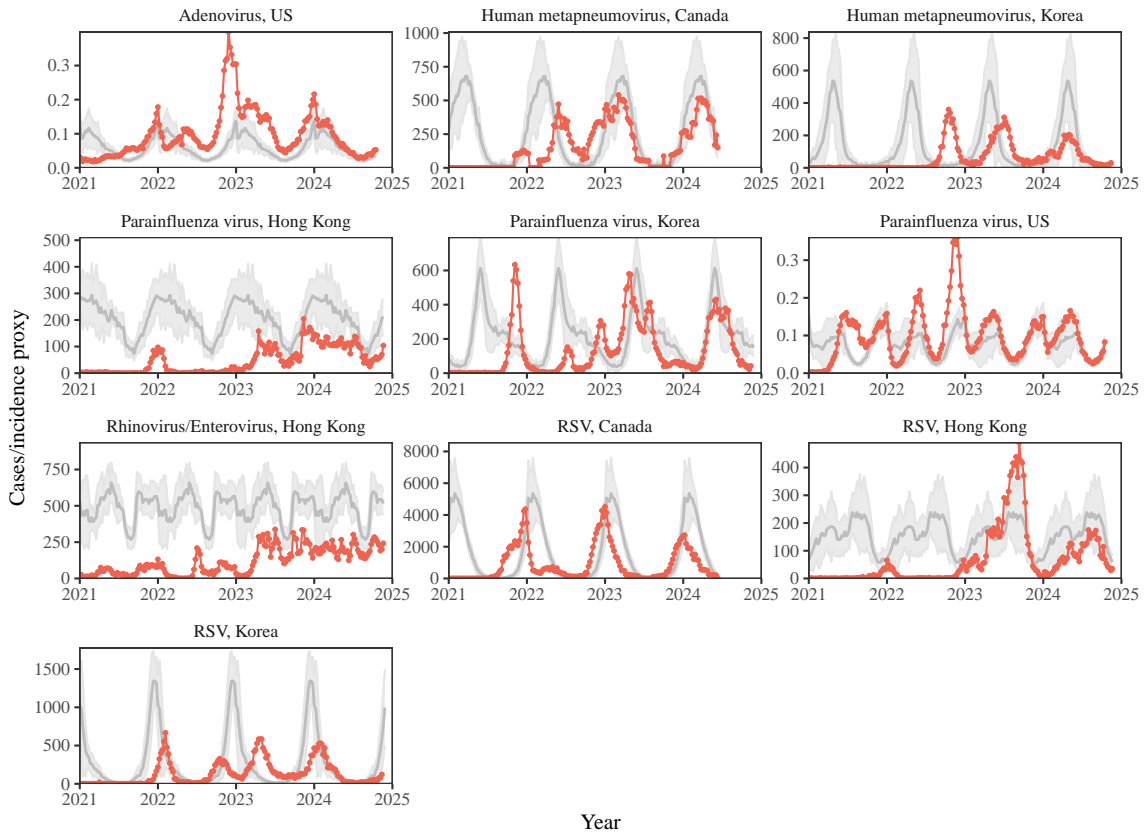


Figure S10: Observed dynamics for pathogen that are predicted to return after the end of 2024. Red points and lines represent data before 2020. Gray lines and shaded regions represent the mean seasonal patterns and corresponding 95% confidence intervals around the mean, previously shown in Figure 1.

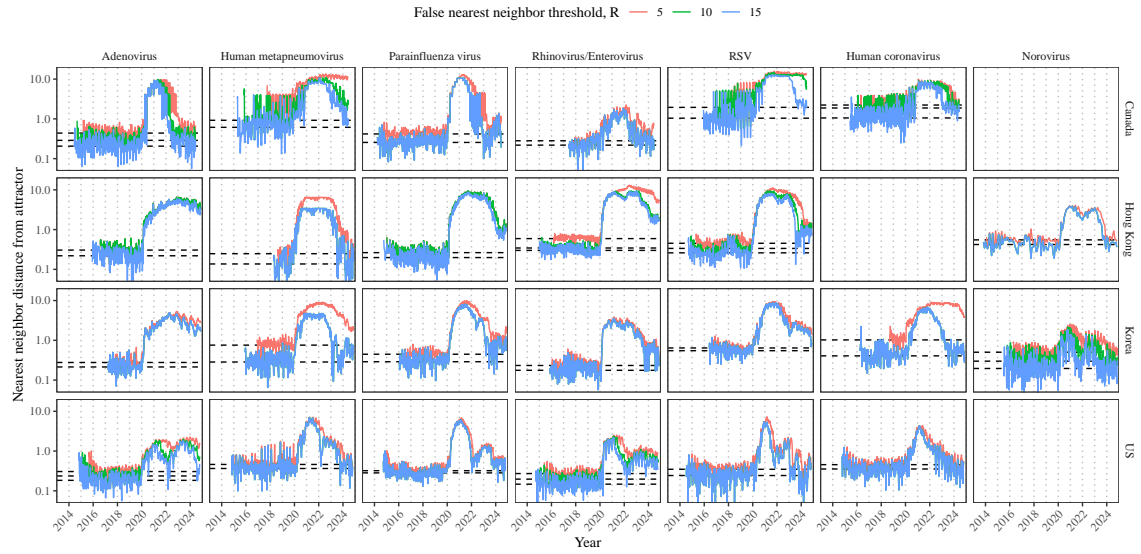


Figure S11: Estimated time series of distance from the attractor for each pathogen across different choices about false nearest neighbor threshold values. Using higher threshold values for the false nearest neighbor approach gives lower embedding dimensions. Colored lines represent the estimated distance from the attractor for different threshold values.

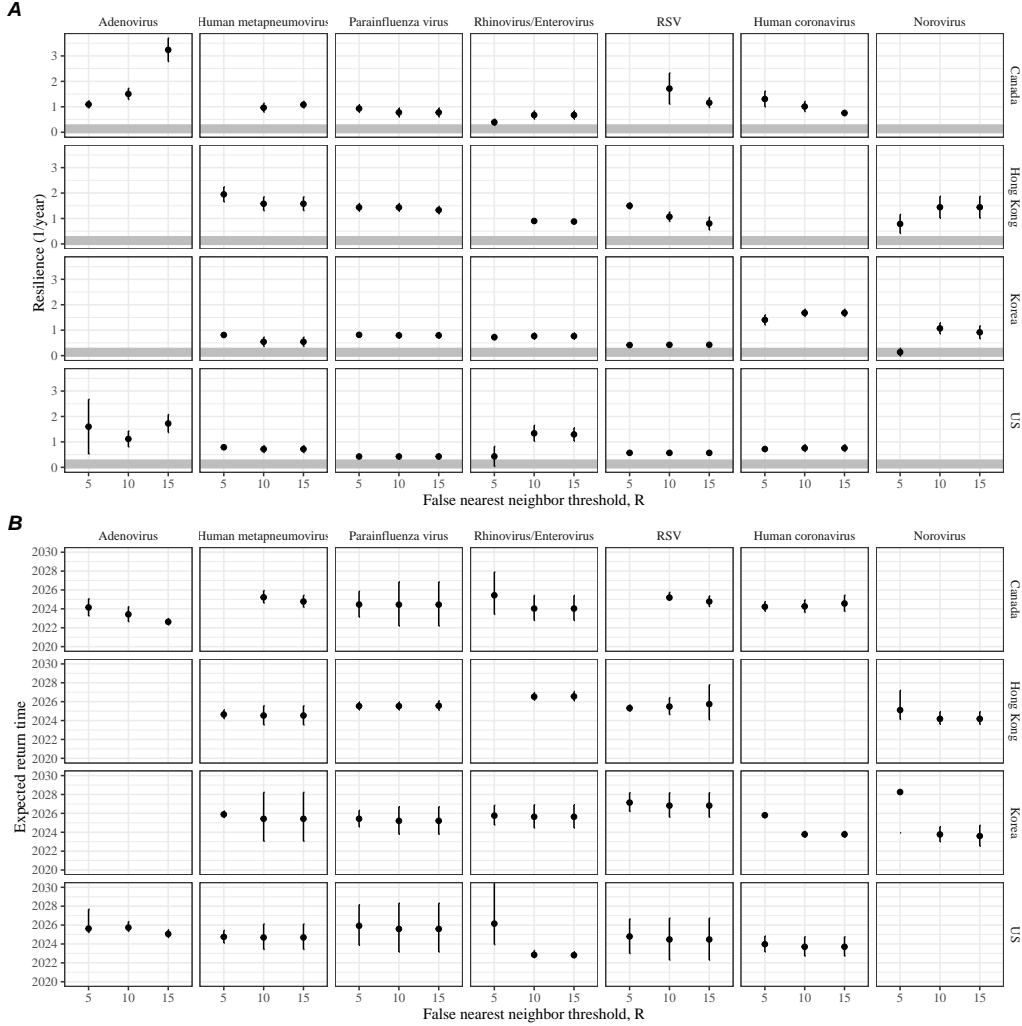


Figure S12: **Summary of resilience estimates and predictions for return time across different choices about false nearest neighbor threshold values.** The automated window selection method was used for all scenarios to estimate pathogen resilience, except for norovirus in Hong Kong and Korea and Rhinovirus/rhinovirus/Enterovirus/enterovirus in the US. We used the same ad-hoc regression windows for norovirus in Hong Kong and Korea and Rhinovirus/rhinovirus/Enterovirus/enterovirus in the US as we did in the main analysis. (A) Estimated pathogen resilience. The gray horizontal line represents the intrinsic resilience of pre-vaccination measles dynamics. (B) Predicted timing of when each pathogen will return to their pre-pandemic cycles. The dashed line in panel B indicates the end of 2024 (current observation time). Error bars represent 95% confidence intervals.

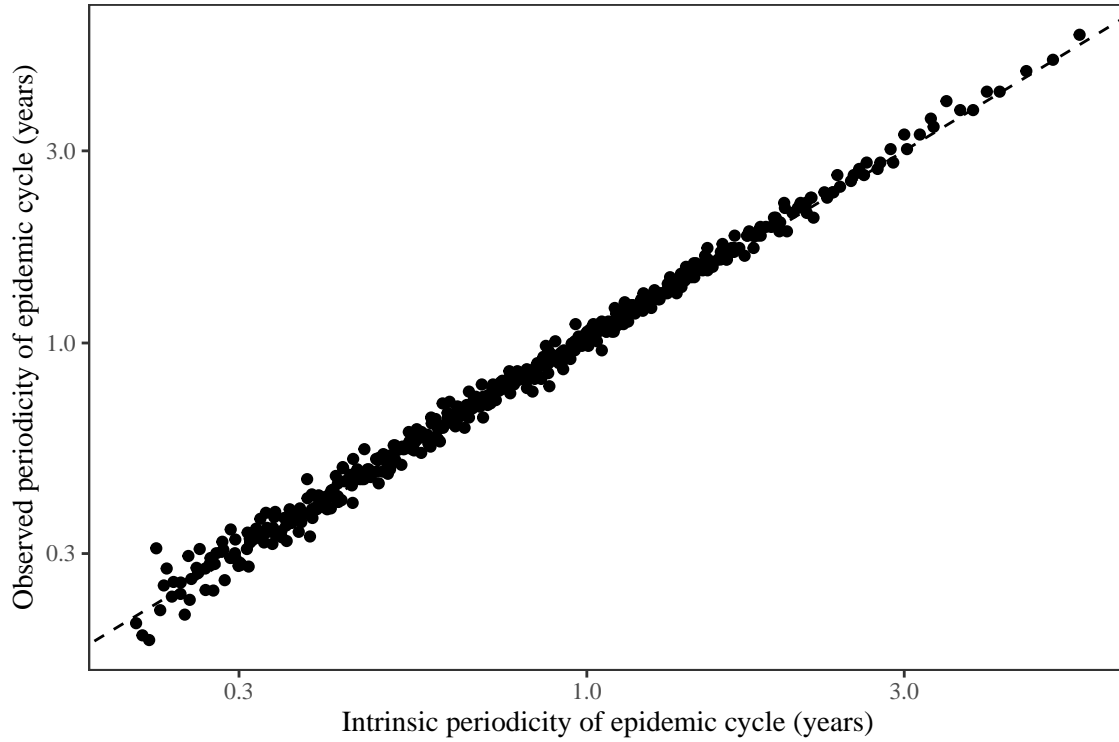


Figure S13: ~~Comparison between the observed and predicted periodicity of the epidemic cycle of the seasonally unforced SIRS model.~~ Comparison between the observed and intrinsic periodicity of the epidemic cycle of the seasonally unforced SIRS model. The observed periodicity of the epidemic corresponds to the periodicity at which maximum spectral density occurs. The ~~predicted intrinsic~~ periodicity of the epidemic corresponds to $2\pi/\text{Im}(\lambda)$, where $\text{Im}(\lambda)$ is the imaginary part of the eigenvalue.

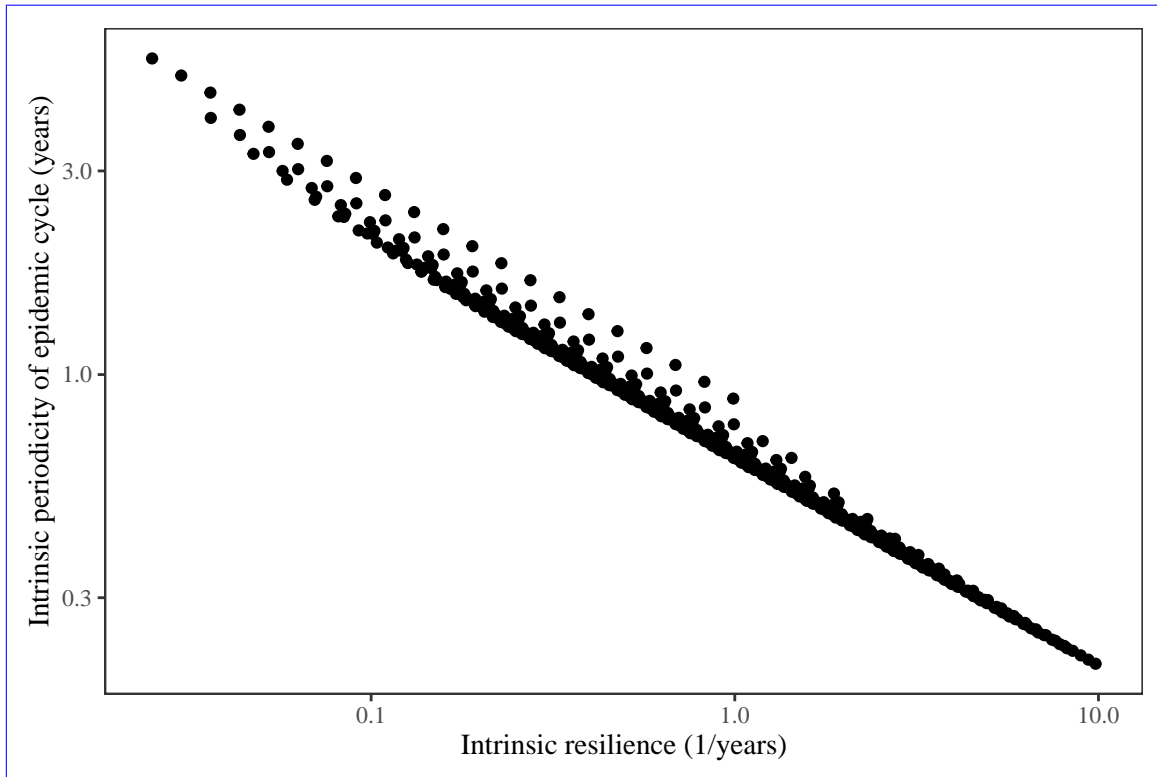


Figure S14: Comparison between the intrinsic resilience and periodicity of the epidemic cycle of the seasonally unforced SIRS model. The intrinsic resilience of the epidemic corresponds to the negative of the real value of the eigenvalue $-\text{Re}(\lambda)$. The intrinsic periodicity of the epidemic corresponds to $2\pi/\text{Im}(\lambda)$, where $\text{Im}(\lambda)$ is the imaginary part of the eigenvalue.

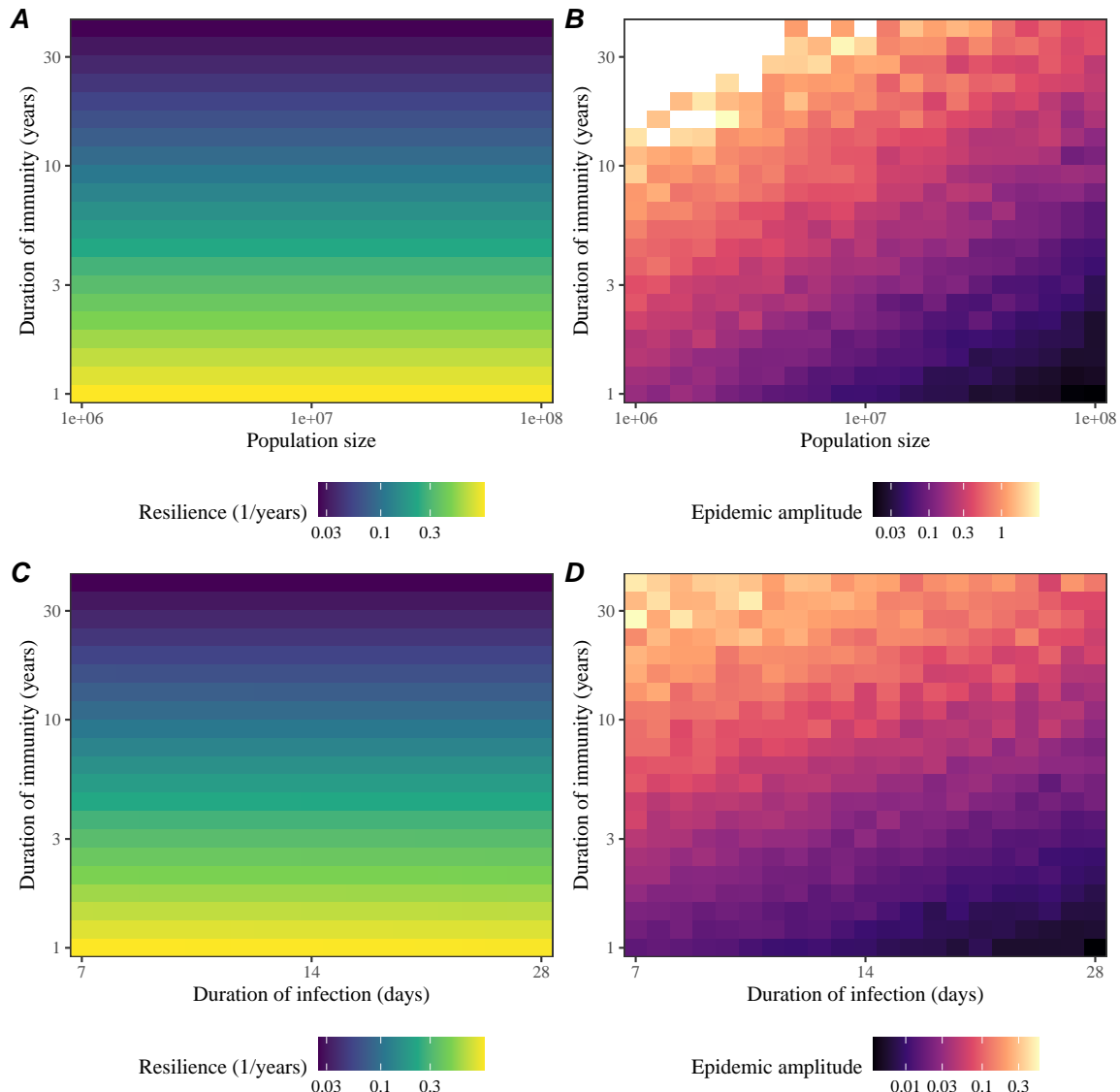


Figure S15: **Impact of population size and the average duration of infection of a host-pathogen system on its sensitivity to stochastic perturbations.** (A) Intrinsic resilience of a system as a function of population size and the average duration of immunity. (B) Epidemic amplitude as a function of population size and the average duration of immunity. (C) Intrinsic resilience of a system as a function of the average duration of infection and immunity. (D) Epidemic amplitude as a function of the average duration of infection and immunity. The epidemic amplitude corresponds to $(\max I - \min I)/(2\bar{I})$, where \bar{I} represents the mean prevalence.

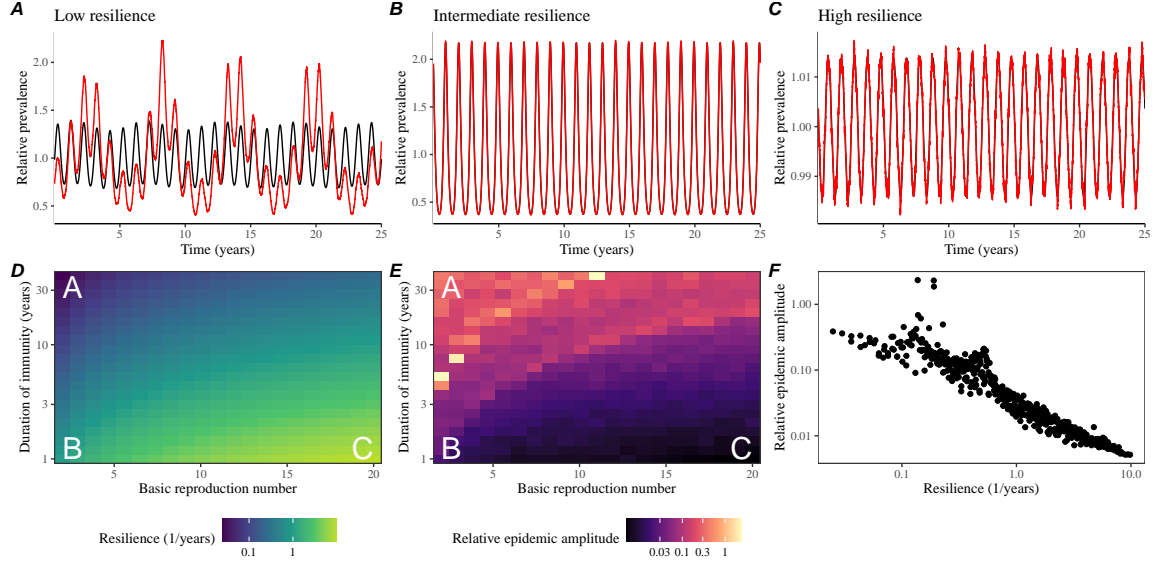


Figure S16: Linking resilience of a host-pathogen system to its sensitivity to stochastic perturbations for the seasonally forced SIRS model. (A–C) Epidemic trajectories of a stochastic SIRS model [with demographic stochasticity](#) across three different resilience values: low, intermediate, and high. The relative prevalence was calculated by dividing infection prevalence by its mean value. [Black lines represent deterministic epidemic trajectories. Red lines represent stochastic epidemic trajectories.](#) (D) The [heat map represents the](#) intrinsic resilience of the seasonally unforced system as a function of the basic reproduction number \mathcal{R}_0 and the duration of immunity. (E) The [heat map represents the](#) relative epidemic amplitude, [a measure of sensitivity to stochastic perturbations](#), as a function of the basic reproduction number \mathcal{R}_0 and the duration of immunity. To calculate the relative epidemic amplitude, we first take the relative difference in infection prevalence between stochastic and deterministic trajectories: $\epsilon = (I_{\text{stoch}} - I_{\text{det}})/I_{\text{det}}$. Then, we calculate the difference between maximum and minimum of the relative difference and divide by half: $(\max \epsilon - \min \epsilon)/2$. [Labels A–C in panels D and E correspond to scenarios shown in panels A–C.](#) (F) The relationship between pathogen resilience and relative epidemic amplitude.

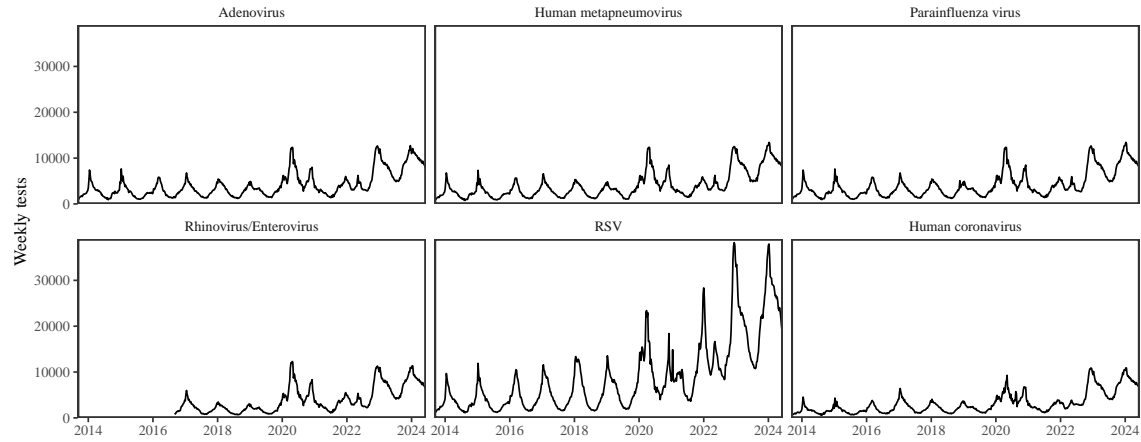


Figure S17: Testing patterns for respiratory pathogens in Canada.

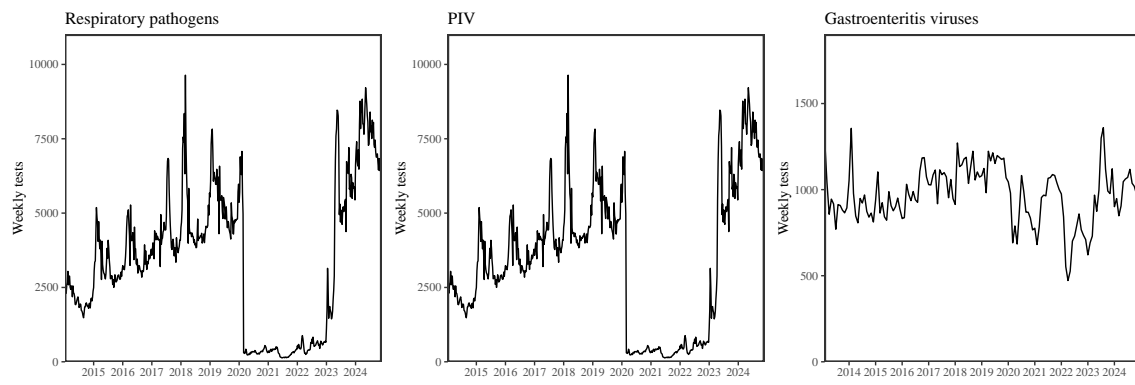


Figure S18: Testing patterns for respiratory pathogens, PIV, and gastroenteritis viruses in Hong Kong.

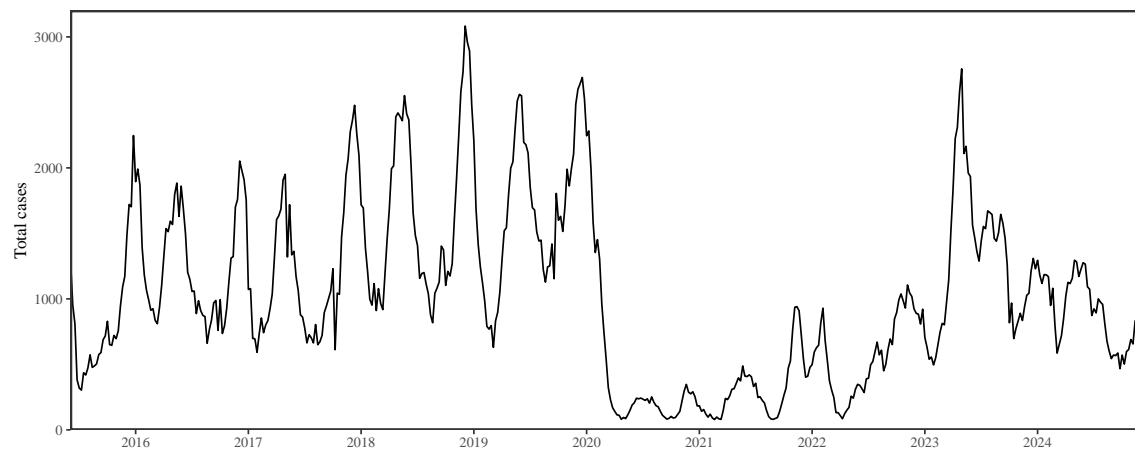


Figure S19: Total number of reported respiratory infection cases in Korea.

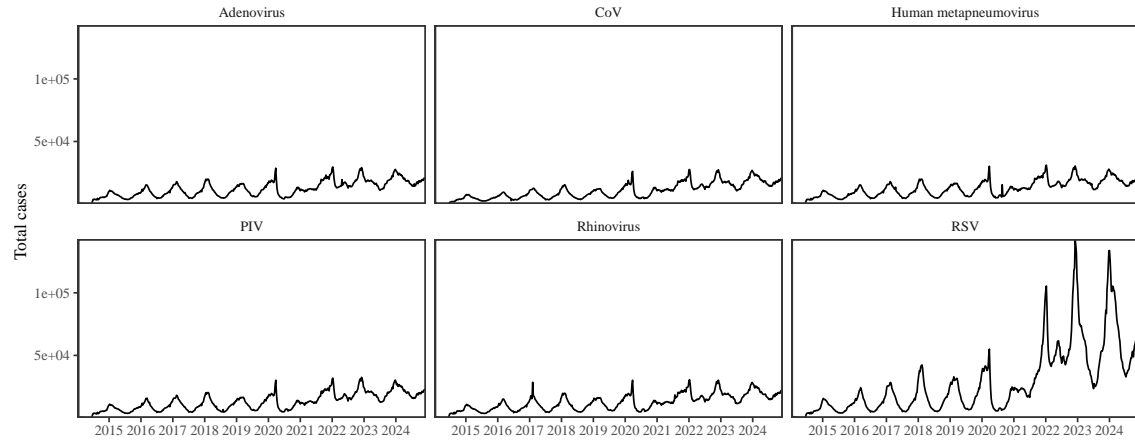


Figure S20: Testing patterns for respiratory pathogens in the US reported through the NREVSS.

878 References

- 879 [1] Rachel E Baker, Sang Woo Park, Wenchang Yang, Gabriel A Vecchi, C Jessica E
880 Metcalf, and Bryan T Grenfell. The impact of COVID-19 nonpharmaceutical
881 interventions on the future dynamics of endemic infections. *Proceedings of the*
882 *National Academy of Sciences*, 117(48):30547–30553, 2020.
- 883 [2] Gabriela B Gomez, Cedric Mahé, and Sandra S Chaves. Uncertain effects of the
884 pandemic on respiratory viruses. *Science*, 372(6546):1043–1044, 2021.
- 885 [3] Mihaly Koltai, Fabienne Krauer, David Hodgson, Edwin van Leeuwen, Marina
886 Treskova-Schwarzbach, Mark Jit, and Stefan Flasche. Determinants of RSV
887 epidemiology following suppression through pandemic contact restrictions. *Epi-*
888 *demics*, 40:100614, 2022.
- 889 [4] Sang Woo Park, Brooklyn Noble, Emily Howerton, Bjarke F Nielsen, Sarah
890 Lentz, Lilliam Ambroggio, Samuel Dominguez, Kevin Messacar, and Bryan T
891 Grenfell. Predicting the impact of non-pharmaceutical interventions against
892 COVID-19 on *Mycoplasma pneumoniae* in the United States. *Epidemics*,
893 49:100808, 2024.
- 894 [5] Amanda C Perofsky, Chelsea L Hansen, Roy Burstein, Shanda Boyle, Robin
895 Prentice, Cooper Marshall, David Reinhart, Ben Capodanno, Melissa Truong,
896 Kristen Schwabe-Fry, et al. Impacts of human mobility on the citywide trans-
897 mission dynamics of 18 respiratory viruses in pre-and post-COVID-19 pandemic
898 years. *Nature communications*, 15(1):4164, 2024.
- 899 [6] Eric J Chow, Timothy M Uyeki, and Helen Y Chu. The effects of the COVID-19
900 pandemic on community respiratory virus activity. *Nature Reviews Microbiol-*
901 *ogy*, 21(3):195–210, 2023.
- 902 [7] Stephen M Kissler, Christine Tedijanto, Edward Goldstein, Yonatan H Grad,
903 and Marc Lipsitch. Projecting the transmission dynamics of SARS-CoV-2
904 through the postpandemic period. *Science*, 368(6493):860–868, 2020.
- 905 [8] Rachel E Baker, Chadi M Saad-Roy, Sang Woo Park, Jeremy Farrar, C Jessica E
906 Metcalf, and Bryan T Grenfell. Long-term benefits of nonpharmaceutical inter-
907 ventions for endemic infections are shaped by respiratory pathogen dynamics.
908 *Proceedings of the National Academy of Sciences*, 119(49):e2208895119, 2022.
- 909 [9] Maaike C Swets, Clark D Russell, Ewen M Harrison, Annemarie B Docherty,
910 Nazir Lone, Michelle Girvan, Hayley E Hardwick, Leonardus G Visser, Pe-
911 ter JM Openshaw, Geert H Groeneveld, et al. SARS-CoV-2 co-infection with
912 influenza viruses, respiratory syncytial virus, or adenoviruses. *The Lancet*,
913 399(10334):1463–1464, 2022.

- 914 [10] Chun-Yang Lin, Joshua Wolf, David C Brice, Yilun Sun, Macauley Locke,
915 Sean Cherry, Ashley H Castellaw, Marie Wehenkel, Jeremy Chase Crawford,
916 Veronika I Zarnitsyna, et al. Pre-existing humoral immunity to human common
917 cold coronaviruses negatively impacts the protective SARS-CoV-2 antibody re-
918 sponse. *Cell host & microbe*, 30(1):83–96, 2022.
- 919 [11] Sam M Murray, Azim M Ansari, John Frater, Paul Klenerman, Susanna
920 Dunachie, Eleanor Barnes, and Ane Ogbe. The impact of pre-existing cross-
921 reactive immunity on SARS-CoV-2 infection and vaccine responses. *Nature*
922 *Reviews Immunology*, 23(5):304–316, 2023.
- 923 [12] John-Sebastian Eden, Chisha Sikazwe, Ruopeng Xie, Yi-Mo Deng, Sheena G
924 Sullivan, Alice Michie, Avram Levy, Elena Cutmore, Christopher C Blyth,
925 Philip N Britton, et al. Off-season RSV epidemics in Australia after easing
926 of COVID-19 restrictions. *Nature communications*, 13(1):2884, 2022.
- 927 [13] Stuart L Pimm. The structure of food webs. *Theoretical population biology*,
928 16(2):144–158, 1979.
- 929 [14] Michael G Neubert and Hal Caswell. Alternatives to resilience for measuring
930 the responses of ecological systems to perturbations. *Ecology*, 78(3):653–665,
931 1997.
- 932 [15] Lance H Gunderson. Ecological resilience—in theory and application. *Annual*
933 *review of ecology and systematics*, 31(1):425–439, 2000.
- 934 [16] Vasilis Dakos and Sonia Kéfi. Ecological resilience: what to measure and how.
935 *Environmental Research Letters*, 17(4):043003, 2022.
- 936 [17] Floris Takens. Detecting strange attractors in turbulence. In *Dynamical Sys-*
937 *tems and Turbulence, Warwick 1980: proceedings of a symposium held at the*
938 *University of Warwick 1979/80*, pages 366–381. Springer, 2006.
- 939 [18] Jonathan Dushoff, Joshua B Plotkin, Simon A Levin, and David JD Earn.
940 Dynamical resonance can account for seasonality of influenza epidemics. *Pro-*
941 , 101(48):16915–16916, 2004.
- 942 [19] Alan Hastings, Carole L Hom, Stephen Ellner, Peter Turchin, and H Charles J
943 Godfray. Chaos in ecology: is mother nature a strange attractor? *Annual review*
944 *of ecology and systematics*, pages 1–33, 1993.
- 945 [20] Alan Hastings, Karen C Abbott, Kim Cuddington, Tessa Francis, Gabriel Gell-
946 ner, Ying-Cheng Lai, Andrew Morozov, Sergei Petrovskii, Katherine Scran-
947 ton, and Mary Lou Zeeman. Transient phenomena in ecology. *Science*,
948 361(6406):eaat6412, 2018.

- 949 [21] Matthew B Kennel, Reggie Brown, and Henry DI Abarbanel. Determining
950 embedding dimension for phase-space reconstruction using a geometrical con-
951 struction. *Physical review A*, 45(6):3403, 1992.
- 952 [22] Eugene Tan, Shannon Algar, Débora Corrêa, Michael Small, Thomas Stemler,
953 and David Walker. Selecting embedding delays: An overview of embedding
954 techniques and a new method using persistent homology. *Chaos: An Interdis-*
955 *ciplinary Journal of Nonlinear Science*, 33(3), 2023.
- 956 [23] Bjarke Frost Nielsen, Sang Woo Park, Emily Howerton, Olivia Frost Lorentzen,
957 Mogens H Jensen, and Bryan T Grenfell. Complex multiannual cycles of My-
958 coplasma pneumoniae: persistence and the role of stochasticity. *arXiv*, 2025.
- 959 [24] Samantha Bosis, Susanna Esposito, HGM Niesters, GV Zuccotti, G Marseglia,
960 Marcello Lanari, Giovanna Zuin, C Pelucchi, ADME Osterhaus, and Nicola
961 Principi. Role of respiratory pathogens in infants hospitalized for a first episode
962 of wheezing and their impact on recurrences. *Clinical microbiology and infection*,
963 14(7):677–684, 2008.
- 964 [25] Miguel L O’Ryan, Yalda Lucero, Valeria Prado, María Elena Santolaya, Marcela
965 Rabello, Yanahara Solis, Daniela Berriós, Miguel A O’Ryan-Soriano, Hector
966 Cortés, and Nora Mamani. Symptomatic and asymptomatic rotavirus and
967 norovirus infections during infancy in a Chilean birth cohort. *The Pediatric
968 infectious disease journal*, 28(10):879–884, 2009.
- 969 [26] Virginia E Pitzer, Cécile Viboud, Vladimir J Alonso, Tanya Wilcox, C Jessica
970 Metcalf, Claudia A Steiner, Amber K Haynes, and Bryan T Grenfell. Environmental
971 drivers of the spatiotemporal dynamics of respiratory syncytial virus in
972 the United States. *PLoS pathogens*, 11(1):e1004591, 2015.
- 973 [27] Arthur WD Edridge, Joanna Kaczorowska, Alexis CR Hoste, Margreet Bakker,
974 Michelle Klein, Katherine Loens, Maarten F Jebbink, Amy Matser, Cormac M
975 Kinsella, Paloma Rueda, et al. Seasonal coronavirus protective immunity is
976 short-lasting. *Nature medicine*, 26(11):1691–1693, 2020.
- 977 [28] Jennifer M Radin, Anthony W Hawksworth, Peter E Kammerer, Melinda Bal-
978 ansay, Rema Raman, Suzanne P Lindsay, and Gary T Brice. Epidemiology
979 of pathogen-specific respiratory infections among three US populations. *PLoS
980 One*, 9(12):e114871, 2014.
- 981 [29] Guojian Lv, Limei Shi, Yi Liu, Xuecheng Sun, and Kai Mu. Epidemiological
982 characteristics of common respiratory pathogens in children. *Scientific Reports*,
983 14(1):16299, 2024.
- 984 [30] Saverio Caini, Adam Meijer, Marta C Nunes, Laetitia Henaff, Malaika Zounon,
985 Bronke Boudewijns, Marco Del Riccio, and John Paget. Probable extinction of

- 986 influenza b/yamagata and its public health implications: a systematic literature
987 review and assessment of global surveillance databases. *The Lancet Microbe*,
988 2024.
- 989 [31] Zhiyuan Chen, Joseph L-H Tsui, Bernardo Gutierrez, Simon Busch Moreno,
990 Louis du Plessis, Xiaowei Deng, Jun Cai, Sumali Bajaj, Marc A Suchard,
991 Oliver G Pybus, et al. COVID-19 pandemic interventions reshaped the global
992 dispersal of seasonal influenza viruses. *Science*, 386(6722):eadq3003, 2024.
- 993 [32] Hai Nguyen-Tran, Sang Woo Park, Kevin Messacar, Samuel R Dominguez,
994 Matthew R Vogt, Sallie Permar, Perdita Permaul, Michelle Hernandez, Daniel C
995 Douek, Adrian B McDermott, et al. Enterovirus D68: a test case for the use of
996 immunological surveillance to develop tools to mitigate the pandemic potential
997 of emerging pathogens. *The Lancet Microbe*, 3(2):e83–e85, 2022.
- 998 [33] Bryan T Grenfell, Ottar N Bjørnstad, and Bärbel F Finkenstädt. Dynamics of
999 measles epidemics: scaling noise, determinism, and predictability with the TSIR
1000 model. *Ecological monographs*, 72(2):185–202, 2002.
- 1001 [34] Samit Bhattacharyya, Per H Gesteland, Kent Korgenski, Ottar N Bjørnstad,
1002 and Frederick R Adler. Cross-immunity between strains explains the dynamical
1003 pattern of paramyxoviruses. *Proceedings of the National Academy of Sciences*,
1004 112(43):13396–13400, 2015.
- 1005 [35] Katharine R Dean, Fabienne Krauer, Lars Walløe, Ole Christian Lingjærde, Bar-
1006 Barbara Bramanti, Nils Chr Stenseth, and Boris V Schmid. Human ectoparasites
1007 and the spread of plague in Europe during the Second Pandemic. *Proceedings
1008 of the National Academy of Sciences*, 115(6):1304–1309, 2018.
- 1009 [36] Margarita Pons-Salort and Nicholas C Grassly. Serotype-specific immunity
1010 explains the incidence of diseases caused by human enteroviruses. *Science*,
1011 361(6404):800–803, 2018.
- 1012 [37] Sarah Cobey and Edward B Baskerville. Limits to causal inference with state-
1013 space reconstruction for infectious disease. *PloS one*, 11(12):e0169050, 2016.
- 1014 [38] P Rohani, CJ Green, NB Mantilla-Beniers, and Bryan T Grenfell. Ecological
1015 interference between fatal diseases. *Nature*, 422(6934):885–888, 2003.
- 1016 [39] Sema Nickbakhsh, Colette Mair, Louise Matthews, Richard Reeve, Paul CD
1017 Johnson, Fiona Thorburn, Beatrix Von Wissmann, Arlene Reynolds, James
1018 McMenamin, Rory N Gunson, et al. Virus–virus interactions impact the popu-
1019 lation dynamics of influenza and the common cold. *Proceedings of the National
1020 Academy of Sciences*, 116(52):27142–27150, 2019.

- 1021 [40] Neil Ferguson, Roy Anderson, and Sunetra Gupta. The effect of antibody-
1022 dependent enhancement on the transmission dynamics and persistence of
1023 multiple-strain pathogens. *Proceedings of the National Academy of Sciences*,
1024 96(2):790–794, 1999.
- 1025 [41] Public Health Agency of Canada. Respiratory virus detections in
1026 Canada. 2024. <https://www.canada.ca/en/public-health/services/surveillance/respiratory-virus-detections-canada.html>. Accessed Sep
1027 4, 2024.
- 1029 [42] Centre for Health Protection. Detection of pathogens from respiratory spec-
1030 imens. 2024. <https://www.chp.gov.hk/en/statistics/data/10/641/642/2274.html>. Accessed Nov 20, 2024.
- 1032 [43] Centre for Health Protection. Detection of gastroenteritis viruses from faecal
1033 specimens. 2024. <https://www.chp.gov.hk/en/statistics/data/10/641/717/3957.html>. Accessed Nov 20, 2024.
- 1035 [44] Korea Disease Control and Prevention Agency. Acute respiratory infection,
1036 Sentinel surveillance infectious diseases. 2024. <https://dportal.kdca.go.kr/pot/is/st/ari.do>. Accessed Nov 20, 2024.
- 1038 [45] Edward Goldstein, Sarah Cobey, Saki Takahashi, Joel C Miller, and Marc Lipsitch.
1039 Predicting the epidemic sizes of influenza A/H1N1, A/H3N2, and B: a
1040 statistical method. *PLoS medicine*, 8(7):e1001051, 2011.
- 1041 [46] Karline Soetaert, Thomas Petzoldt, and R Woodrow Setzer. Solving differential
1042 equations in R: package deSolve. *Journal of statistical software*, 33:1–25, 2010.
- 1043 [47] R Core Team. *R: A Language and Environment for Statistical Computing*. R
1044 Foundation for Statistical Computing, Vienna, Austria, 2023.
- 1045 [48] Sang Woo Park, Inga Holmdahl, Emily Howerton, Wenchang Yang, Rachel E
1046 Baker, Gabriel A Vecchi, Sarah Cobey, C Jessica E Metcalf, and Bryan T Grenfell.
1047 Interplay between climate, childhood mixing, and population-level suscep-
1048 tibility explains a sudden shift in RSV seasonality in Japan. *medRxiv*, pages
1049 2025–03, 2025.
- 1050 [49] Bob Carpenter, Andrew Gelman, Matthew D Hoffman, Daniel Lee, Ben
1051 Goodrich, Michael Betancourt, Marcus A Brubaker, Jiqiang Guo, Peter Li,
1052 and Allen Riddell. Stan: A probabilistic programming language. *Journal of
1053 statistical software*, 76, 2017.
- 1054 [50] Stan Development Team. RStan: the R interface to Stan, 2024. R package
1055 version 2.32.6.